



This is a repository copy of *Integration of energy and electron transfer processes in the photosynthetic membrane of Rhodobacter sphaeroides*.

White Rose Research Online URL for this paper:
<http://eprints.whiterose.ac.uk/110824/>

Version: Accepted Version

Article:

Cartron, M.L., Olsen, J.D., Sener, M. et al. (7 more authors) (2014) Integration of energy and electron transfer processes in the photosynthetic membrane of *Rhodobacter sphaeroides*. *Biochimica et Biophysica Acta (BBA) - Bioenergetics*, 1837 (10). pp. 1769-1780. ISSN 0005-2728

<https://doi.org/10.1016/j.bbabi.2014.02.003>

Article available under the terms of the CC-BY-NC-ND licence
(<https://creativecommons.org/licenses/by-nc-nd/4.0/>)

Reuse

This article is distributed under the terms of the Creative Commons Attribution-NonCommercial-NoDerivs (CC BY-NC-ND) licence. This licence only allows you to download this work and share it with others as long as you credit the authors, but you can't change the article in any way or use it commercially. More information and the full terms of the licence here: <https://creativecommons.org/licenses/>

Takedown

If you consider content in White Rose Research Online to be in breach of UK law, please notify us by emailing eprints@whiterose.ac.uk including the URL of the record and the reason for the withdrawal request.



eprints@whiterose.ac.uk
<https://eprints.whiterose.ac.uk/>

Published in final edited form as:

Biochim Biophys Acta. 2014 October ; 1837(10): 1769–1780. doi:10.1016/j.bbabi.2014.02.003.

Integration of energy and electron transfer processes in the photosynthetic membrane of *Rhodobacter sphaeroides*

Michaël L. Cartron^a, John D. Olsen^a, Melih Sener^{b,c}, Philip J. Jackson^{a,d}, Amanda A. Brindley^a, Pu Qian^a, Mark J. Dickman^d, Graham J. Leggett^e, Klaus Schulten^{b,c,f}, and C. Neil Hunter^{a,*}

^aDepartment of Molecular Biology and Biotechnology, University of Sheffield, Sheffield S10 2TN, United Kingdom

^bBeckman Institute for Advanced Science and Technology, University of Illinois at Urbana-Champaign, Urbana, Illinois 61801

^cDepartment of Physics, University of Illinois at Urbana-Champaign, Urbana, Illinois 61801

^dChELSI Institute, Department of Chemical and Biological Engineering, University of Sheffield, Mappin Street, Sheffield, S1 3JD, United Kingdom

^eDepartment of Chemistry, University of Sheffield, Brook Hill, Sheffield S3 7HF, UK

^fCenter for Biophysics and Computational Biology, University of Illinois at Urbana-Champaign, Urbana, Illinois 61801

Abstract

Photosynthesis converts absorbed solar energy to a protonmotive force, which drives ATP synthesis. The membrane network of chlorophyll–protein complexes responsible for light absorption, photochemistry and quinol (QH₂) production has been mapped in the purple phototrophic bacterium *Rhodobacter (Rba.) sphaeroides* using atomic force microscopy (AFM), but the membrane location of the cytochrome *bc*₁ (*cytbc*₁) complexes that oxidise QH₂ to quinone (Q) to generate a protonmotive force is unknown. We labelled *cytbc*₁ complexes with gold nanobeads, each attached by a Histidine₁₀ (His₁₀)-tag to the C-terminus of *cytc*₁. Electron microscopy (EM) of negatively stained chromatophore vesicles showed that the majority of the *cytbc*₁ complexes occur as dimers in the membrane. The *cytbc*₁ complexes appeared to be adjacent to reaction centre light-harvesting 1-PufX (RC-LH1-PufX) complexes, consistent with AFM topographs of a gold-labelled membrane. His-tagged *cytbc*₁ complexes were retrieved from chromatophores partially solubilised by detergent; RC-LH1-PufX complexes tended to co-purify with *cytbc*₁, whereas LH2 complexes became detached, consistent with clusters of *cytbc*₁ complexes close to RC-LH1-PufX arrays, but not with a fixed, stoichiometric *cytbc*₁-RC-LH1-PufX supercomplex. This information was combined with a quantitative mass spectrometry (MS) analysis of the RC, *cytbc*₁, ATP synthase, *cytaa*₃ and *cytcb*₃ membrane protein complexes, to

*Corresponding author: Department of Molecular Biology and Biotechnology, University of Sheffield, Sheffield S10 2TN, United Kingdom. c.n.hunter@sheffield.ac.uk. Tel.: +44 114 222 4191. Fax +44 114 222 2711.

Author Contributions M.L.C., J.D.O., M.S., P.J.J., A.A.B. and P.Q. designed and performed experiments, M.S. and K.S. did the modelling/computational work, C.N.H., J.D.O., M.L.C., P.J.J., M.J.D., G.J.L., M.K.S., and K.S. wrote the paper. M.L.C. and J.D.O. contributed equally to the work.

construct an atomic-level model of a chromatophore vesicle comprising 67 LH2 complexes, 11 LH1-RC-PufX dimers & 2 RC-LH1-PufX monomers, 4 *cytbc*₁ dimers and 2 ATP synthases. Simulation of the interconnected energy, electron and proton transfer processes showed a half-maximal ATP turnover rate for a light intensity equivalent to only 1% of bright sunlight. Thus, the photosystem architecture of the chromatophore is optimised for growth at low light intensities.

Keywords

bacterial photosynthesis; cytochrome *bc*₁; atomic force microscopy; electron microscopy; quinone; membrane modeling

1. Introduction

Photosynthetically driven cyclic electron transport requires two membrane-bound components in purple bacteria, the RC-LH1 core complex and the *cytbc*₁ complex. In many purple phototrophs energy is absorbed by a third complex, LH2, many copies of which form a peripheral antenna for absorbing and transferring excitation energy to the LH1 complex that surrounds the reaction centre. Excitation of a special pair of bacteriochlorophylls (BChls) within the RC releases an electron that passes rapidly along a series of pigments until it arrives at an exchangeable quinone, Q_B. Successive excitations generate the two electrons necessary to convert the Q_B quinone to a quinol which then undocks from the RC and diffuses through the lipid bilayer to a *cytbc*₁ complex. Here, quinol molecules are oxidised, protons are discharged into the enclosed lumen of the photosynthetic membrane and cytochrome *c*₂, bound to the periplasmic surface of the *cytbc*₁ complex, is reduced. Repeated turnovers of this cyclic system are made possible by the membrane-extrinsic cytochrome *c*₂ and the membrane-intrinsic quinone/quinol (Q/QH₂) molecules, each shuttling between the RC-LH1 and *cytbc*₁ complexes [1]. The same principles, of light harvesting, photochemistry and Q/QH₂ traffic between the RC and a membrane-bound cytochrome complex, apply to most photosynthetic organisms. However, energy migration among LH complexes and Q/QH₂ traffic between RC-LH1 and *cytbc*₁ complexes have conflicting requirements; dense packing of RC-LH1 and LH2 complexes fosters rapid energy transfer, but hinders lateral diffusion of Q/QH₂, effectively weakening the linkage between RC photochemistry and QH₂ oxidation at the Q_o site of the *cytbc*₁ complex. This linkage has been studied using short flashes of light to initiate electron transfer and QH₂ formation, and conflicting models for cyclic electron flow arose from experiments using intracytoplasmic membrane vesicles (‘ chromatophores’) from *Rba. sphaeroides*. Joliot et al. [2] proposed that the RC and *cytbc*₁ form a supercomplex, whereas others, notably Crofts and co-workers [3], explained their results without invoking a fixed structural and functional relationship between RC and the *cytbc*₁ complexes. These opposing concepts for the supramolecular organisation of photosynthetic membranes, derived from kinetic experiments, are equivalent to the ‘ solid state’ and ‘ liquid state’ models proposed by Rich [4].

More recently Comayras and co-workers used a kinetic approach to study the distribution of RCs and quinones in *Rba. sphaeroides*, and concluded that within a chromatophore

membrane there are confined quinone domains associated with up to six reaction centers [5]. Direct structural evidence is now required to determine the membrane location of the *cytc₁* complex in *Rba. sphaeroides*. A previous atomic force microscopy (AFM) study of the *Rba. sphaeroides* photosynthetic membrane [6] showed that dimeric RC-LH1-PufX ‘cores’ are connected to large arrays of closely-packed LH2 complexes but *cytc₁* complexes were not detected; the *cytc₁* structure [7] shows that the cytoplasmically-exposed face has very little surface topology to aid its identification by AFM, and the cytoplasmic side of the membrane is generally the only side observed in such experiments. Here, we have used a combination of electron microscopy (EM) and AFM to identify *cytc₁* complexes and determine their location and aggregation state in a chromatophore vesicle. We overcame the membrane topology problem by attaching a Histidine₁₀ (His₁₀)-tag to the C-terminus of *cytc₁*, which enabled labelling by Nanogold[®] beads functionalised with Ni-nitrilotriacetic acid (Ni-NTA) groups and pulldown experiments to examine *cytc₁*-RC-LH1-PufX associations. This new mapping information, together with quantitative mass spectrometry and membrane modelling, has allowed computation of energy conversion efficiencies for an atomic-level chromatophore vesicle.

2. Materials and methods

2.1. Growth of *Rba. sphaeroides* and conjugative transfer of pK18mobsacB

The strains used in this study were (1) *Rba. sphaeroides* 2.4.1 wild type, (2) *Rba. sphaeroides* BC1C10H (*fbcC*::thrombin-His₁₀), (3) *Escherichia (E.) coli* S17-1 [8], (4) *E. coli* Rosetta II, pLysS (Novagen).

Single colonies of *Rba. sphaeroides* strains were inoculated into 10 ml of M22+ medium and grown for 48 hours at 34°C in the dark with shaking, then 1 ml sub-cultured into 70 ml of M22+ in a 100 ml conical flask and incubated overnight at 34°C with shaking. Further subculturing was used for growth under photosynthetic conditions in volumes up to 20 L.

The vector pK18mobsacB (ATCC[®] 87097TM) was used to introduce the gene encoding the C-terminal His-tagged *cytc₁* into the *Rba. sphaeroides* genome. The flanking regions of 1090bp and 849bp were made by PCR of genomic DNA using the primers listed below:

Primer 1: FbcC BamHI CGGGATCCTGACCTGGGTCGGCG

Primer 2 FbcC SacI GGGGAGAGCTCGTTCGTCTTCTTCTTGCCC

Primer 3 FbcC SalI GGTCGACGAGGACAGGCCCGCTTC

Primer 4 FbcC HindIII CTGAAGCTTCTCGTCCAGCGGCTGATGG

pET52b+ (Novagen) was used to provide the thrombin cleavage site and the 10-His tag which was introduced at the C-terminus of FbcC. The sequence of the C-terminal extension to *cytc₁* was LALVPRGSSAHHHHHHHHHH. pK18mobsacB derivatives were transferred to *Rba. sphaeroides* using the conjugation-competent *E. coli* strain S17-1. Positive mutants were identified using colony PCR.

2.2. Membrane preparation

Cells harvested from a 2.5 L culture were resuspended in 30 ml of membrane buffer (20 mM MOPS, 600 mM NaCl, pH 7), a few grains of DNase I and lysosyme were added to the suspension and the cells were then disrupted in a French pressure cell at 18,000 psi; two cycles of French pressing were used to ensure the majority of cells were disrupted. The lysate was centrifuged at 15,000 rpm for 25 minutes, and the supernatant layered onto a discontinuous 15/40 % (w/w) sucrose density gradient and centrifuged in a Beckman Ti45 rotor at 27,000 rpm ($53,000 \times g$) for 10 hours. The chromatophore band, present just above the 15/40% interface, was collected with a micropipette then stored at 4 °C overnight or frozen at -20°C until required.

2.3. Nanogold labelling of chromatophores and membrane patches

30 μL of $A_{850=27}$ of chromatophores from the *Rba. sphaeroides* BC1C10His-tag mutant were incubated with 200 nM 5 nm Ni-NTA-Nanogold® (Nanoprobes); this concentration minimised a crosslinking effect, whereby Ni-NTA groups on a gold bead interact with more than one His-tagged *cytbc₁* complex and promote formation of vesicle clusters. The membranes and gold beads were incubated in a 50 μL volume for up to 3 hours, then made up to 3 mL with buffer A (20 mM HEPES pH 7.5, 10 mM EDTA) and loaded onto a discontinuous 20%/30%/40%/50% (w/w) sucrose gradient in buffer A, and centrifuged in a Beckman SW41 rotor at 40,000 rpm for 4 hours. The nanogold-labelled bands, present just above the 40–50% interface (Fig. 1), were collected with a micropipette and immediately transferred onto carbon grids, as described above, for EM analysis.

The same procedure was adopted for labeling and isolation of nanogold-labeled membrane patches, except that after the initial 3-hour incubation β -DDM was added to the mix to a final concentration of 0.1 mM, and incubated for an hour. The mix was then layered onto a discontinuous 20%/30%/40%/50% (w/w) sucrose gradient containing 0.025 mM TDM (n-tetradecyl- β -D-maltopyranoside; Anatrace, USA). The resultant patches were analyzed by TEM and AFM.

2.4. Electron microscopy

Samples were applied to glow-discharged carbon coated copper grids and negatively stained with 0.75 % w/v uranyl formate. Images were recorded at 100 kV on a Philips CM100 microscope equipped with a Gatan Ultrascan 667 CCD camera at 61,005X magnification.

2.5. Atomic Force Microscopy

Membrane patches were typically diluted 1:10 in 20 mM HEPES pH 7.5 before adding 5 μL of the diluted suspension to 45 μL of binding buffer, 20 mM HEPES pH 7.5, 150 mM KCl, 25 mM MgCl_2 , on a freshly cleaved mica disk (Agar Scientific). The sample was incubated for ~ 1 hour at RT in a Petri dish with a piece of moistened paper towel to minimise drying. The binding buffer was removed with a pipette and the sample rinsed twice with 50 μL of imaging buffer, 20 mM HEPES pH 7.5, 100 mM KCl. SNL cantilevers, spring constant 0.24 Nm^{-1} , resonant frequency 56 kHz (Bruker), were used in a Nanoscope Multimode 8

(Bruker) in Peakforce QNM imaging mode. Scan speeds were typically 1 Hz or less. The data were analysed and processed using NanoScope Analysis software (Bruker).

2.6. Progressive solubilization of chromatophores and retrieval of His-cyt bc_1 complexes on affinity columns

All steps were performed, as far as possible, at 4°C. Approximately 60 ODU (@ 850 nm) of purified chromatophores in an end volume of 3 ml were used for each concentration of β -DDM (Glycon, Germany). A 10% β -DDM stock was made in buffer A (20 mM MOPS, 600 mM NaCl, pH 7) and the appropriate volume was slowly added to the membrane suspension to achieve final β -DDM concentrations of: 0.1%, 0.5%, 1%, 2% and 2.5%. Following incubation at 4°C with stirring for 40 minutes the samples were loaded onto individual Ni²⁺-NTA columns (5 ml) equilibrated with buffer A. The columns were washed with 2 column volumes of Buffer A, then with sufficient Buffer B (20 mM MOPS, 600 mM NaCl, 20mM imidazole, pH 7) until the flow-through was clear, typically 15 ml, and the sample eluted with buffer C (20 mM MOPS, 600 mM NaCl, 500 mM imidazole, pH 7). The final elution volume was typically around 3.5 ml, of which 200 μ l was immediately transferred to a cuvette and absorbance spectroscopy performed as detailed in the next section. The remaining eluate was used for determination of protein and bacteriochlorophyll concentration, and for quinone and lipid extraction.

Three membrane samples were treated with 0.1, 0.5, 1.0, 2.0, or 2.5% β -DDM detergent, and the extracts fractionated using a total of 15 affinity columns. Each of the three eluates at a given starting detergent concentration was analysed for complexes or extracted for quinones and lipids in duplicate.

2.7. Absorbance spectroscopy

Absorbance spectra of purified chromatophore and membrane fractions were recorded on a Cary 50 UV-Vis spectrophotometer between 250–950 nm. When assessing the levels of the cyt bc_1 complex the absorbance spectrum was recorded, then a few grains of sodium dithionite were added to reduce the samples, and the spectrum re-recorded. The extinction coefficients used were 7430 mM⁻¹ cm⁻¹ for the RC-LH1-PufX complex, 3720 mM⁻¹ cm⁻¹ for LH2³³. The concentrations of *b*- and *c*-type cytochromes were estimated using the extinction coefficients $\epsilon_{561-575}$ of 22 mM⁻¹ cm⁻¹ and $\epsilon_{551-540}$ of 19 mM⁻¹ cm⁻¹, respectively [9]. Baselines were corrected and spectra were processed with Excel/Origin software as required.

2.8. Quinone and lipid extraction

All steps were performed as far as possible at 4°C. Quinones and lipids were extracted following the same protocol. Eight volumes of 50/50 methanol/chloroform were added to one volume of untreated chromatophore vesicles. The mixture was vortexed several times and centrifuged, the colourless pellet was discarded and the coloured methanol/chloroform extract used for the lipid or quinone analysis. This procedure was repeated in triplicate for each sample solubilised with β -DDM.

2.8.1. Lipid analysis—Phospholipids were analysed and quantified according to [10]. All the extracted samples were dried into a glass tube to which was added 0.3 ml 70% perchloric acid, then the tubes were heated in a block for 3 hours at 180°C. 1 ml water, 0.4 ml 1.25 % (w/v) ammonium hepta-molybdate and 0.4 ml of 5% ascorbic acid was then added to each sample, vortexed and incubated for 5 minutes in a 100°C water bath. The tubes were cooled in cold water (4°C) before the absorbance was measured at 797 nm. Each sample was measured in triplicate. Individual phospholipids were separated by thin-layer chromatography and quantified as above, using published methods [11].

2.8.2. Quinone analysis—Quinones were analysed and quantified as described [12] with minor modifications. Quinones were extracted as described above. 50 µl of each sample was loaded onto an Ultrasphere ODS column (Beckman Coulter) and equilibrated with 100% methanol at a flow rate of 1 ml.min⁻¹. HPLC traces were analysed at 260, 270, 280, 290 and 300 nm and the areas under the peaks integrated. The column was calibrated with 5000, 2500, 1250, 625, 312.5, 156.25, 78.1, 39 and 19.5 µg.ml⁻¹ of coenzyme Q10 (Sigma) dissolved in 100% methanol.

2.9. Preparation of ¹⁵N-labelled artificial protein standard

The ¹⁵N-labelled internal standard was constructed as an artificial protein composed of concatenated tryptic peptide sequences [13, 14] that are known to represent the target proteins in proteomic analysis. The N-terminal extension AWSWK was added to increase the absorbance of the artificial protein at 280 nm, thereby enhancing the accuracy of the quantification. The sequence was back-translated into the DNA sequence and optimised for expression in bacteria. The corresponding gene was synthesised (Bio Basic) with N-terminal *NdeI* and C-terminal *BamHI* sites to enable sub-cloning into a pET14b vector (Novagen), incorporating an N-terminal His-tag sequence. *E. coli* (Rosetta II, *pLysS*, Novagen) was grown at 37°C in 1.5 l M9 medium containing (¹⁵NH₄)₂SO₄ (99 atom%, Cambridge Isotope Laboratories) to an OD of 0.7 at 600 nm. Overproduction of the protein was induced by the addition of 0.4 mM IPTG and the culture transferred to 20°C for 16 hours. Cells were pelleted at 4,000 × *g* for 30 minutes at 4°C and then re-suspended in 20 ml IMAC buffer (25 mM Tris/HCl pH 7.4, 300 mM NaCl, 5 mM imidazole). The cells were broken by sonication on ice in 10 × 30-second bursts and the insoluble fraction pelleted by centrifugation at 33,000 × *g* for 30 minutes at 4°C. The pellet was washed in IMAC buffer and re-centrifuged. The insoluble fraction was re-suspended in IMAC buffer containing 8 M urea and sonicated on ice in 10 × 30-sec bursts. The urea extract was stirred for 1 hour at 4°C and clarified by centrifugation at 33,000 × *g* for 30 minutes at 20 °C. The supernatant was applied to a 5 ml Ni²⁺-charged chelating Sepharose column (GE Healthcare) equilibrated in IMAC buffer containing 8 M urea. The column was washed with 50 ml IMAC buffer containing 8 M urea followed by 50 ml IMAC buffer containing 8 M urea and 50 mM imidazole. The ¹⁵N-(His₆)-protein standard was eluted from the column with IMAC buffer containing 8 M urea and 250 mM imidazole and its concentration determined from the calculated molar extinction coefficient at 280 nm (www.expasy.org/protparam/).

2.10. Quantification of proteotypic peptides from subunits of the reaction centre, cytochrome *bc*₁, ATP synthase and terminal cytochrome *c* oxidases by liquid chromatography coupled to mass spectrometry

Chromatophores were buffer exchanged into 50 mM NH₄HCO₃, 0.1 mM DTT, 5 mM MgCl₂ using a PD-10 column (GE Healthcare) and the protein concentration determined at 1.39 mg/ml by Bradford assay. 0.2 ml membrane (278 µg) was mixed with 50 pmol ¹⁵N-labelled artificial protein standard and 11 µg trypsin (proteomics grade, Sigma) in a total volume of 0.8 ml 0.05% ProteaseMax surfactant (Promega) in 50 mM NH₄HCO₃. Digestion was carried out at 48 °C [15] for 6 hours before transfer to 37 °C. 0.2 ml aliquots were removed at 3, 6 and 23 hours and immediately added to 20 µl 5% trifluoroacetic acid (TFA) to stop digestion and hydrolyse the surfactant. After incubation for 5 minutes at RT, samples were centrifuged at 16,000 × *g* for 5 minutes and the supernatant applied to a C₁₈ SpinTip (Protea Biosciences) according to the manufacturer's instructions. The eluted tryptic peptides were dried in a vacuum centrifuge, re-dissolved in 20 µl 0.1% TFA, 3% acetonitrile and 2 µl aliquots (equivalent to 6.95 µg membrane protein and 1.25 pmol ¹⁵N-labelled protein standard) were analysed in duplicate by nanoflow liquid chromatography (Ultimate 3000 RSLCnano, Dionex) coupled to a Maxis UHR-TOF mass spectrometer (Bruker). Peptide separation was performed using 5 mm × 300 µm trapping and 150 mm × 75 µm analytical PepMap C₁₈ reverse-phase columns (Dionex) with linear gradient elution from 4% solvent A (0.1% formic acid in water) to 40% solvent B (0.1% formic acid in 80% acetonitrile) over 90 minutes at 0.3 µl.min⁻¹. Mass spectra were acquired in profile mode with automatic dependent MS/MS scans.

The identities of the tryptic peptides, both unlabelled (from chromatophore) and ¹⁵N-labelled (from the artificial protein standard) counterparts, were confirmed by searching the *Rba. sphaeroides* complete proteome database (ExPASy) using Mascot Server v. 2.2.01 (Matrix Science). DataAnalysis v. 4.0 software (Bruker) was used to extract ion chromatograms for the target peptide ions from the profile MS data and average the spectra across the relevant peaks. The averaged spectra were then processed to display the monoisotopic ion intensity values for each ¹⁴N/¹⁵N pair which enabled the quantification of these peptides (see Table S2).

2.11. Modeling chromatophore structure and function

Placement of light harvesting proteins LH2 and LH1-RC was performed as reported earlier [16, 17] employing the area-preserving inverse-Mollweide transformation to map planar AFM images upon spherical domains and manually adjusting protein locations to remove steric clashes. The size and shape of the vesicle are observed by EM and AFM [18]. The packing density of LH2 domains for the intact vesicle was determined in a previous study [19]. The stacking pattern of RC-LH1-PufX dimers follows the curvature and association profiles observed earlier [17, 20]. The relative spatial associations of *cytbc*₁ and ATP synthase complexes with respect to the LH proteins were determined in accordance with proteomics studies [21] as well as negative stain EM images (Fig. 2–4). The relative stoichiometry of proteins in the chromatophore was established through spectroscopy of the LH pigments [18] as well as from MS data (Table 1).

Electronic excitations that result from photon absorption are quickly delocalized over the pigment cluster of each LH protein. Thermal equilibrium of excited states within each pigment cluster is reached on timescales (< 1 ps) that are shorter than excitation transfer between nearby proteins (~ 5 – 10 ps) [22]. Correspondingly, migration of excitation across pigment clusters is a Markovian process and can be described by the modified Förster formalism [23].

In this formalism, excited states of a pigment cluster I containing N_I pigments are described by an effective Hamiltonian [17]

$$H^I = \sum_{i=1}^{N_I} \varepsilon_i^I |i\rangle \langle i| + \sum_{i>j>0}^{N_I} V_{ij}^I (|i\rangle \langle j| + |j\rangle \langle i|), \quad (1)$$

where $|i\rangle$ are the Q_y -states of individual BChls forming a basis for H^I . The rate of excitation transfer between a donor pigment cluster D and an acceptor pigment cluster A is given by the modified Förster formula (see [23] for a review)

$$k_{DA} = \frac{2\pi}{\hbar} \sum_{m \in D} \sum_{n \in A} e^{-\beta \varepsilon_m} \left| \langle \tilde{n} | H_{DA} | \tilde{m} \rangle \right|^2 J_{mn} / \sum_{p \in D} e^{-\beta \varepsilon_p}, \quad (2)$$

where $|\tilde{m}\rangle$ and $|\tilde{n}\rangle$ are the eigenstates for the effective Hamiltonians H^D and H^A , given by eq. (1), corresponding to the donor and acceptor clusters, D and A , respectively; J_{mn} are spectral overlaps in units of 1/energy; ε_m are eigenvalues of H^D for pigment cluster D , given by $H^D |\tilde{m}\rangle = \varepsilon_m |\tilde{m}\rangle$ and H_{DA} is the matrix of cross-couplings between pigments of clusters D and A . Excitation transfer across the chromatophore is subsequently governed by a first order kinetics matrix K constructed from the inter-cluster transfer rates k_{DA} according to

$$(K)_{IJ} = k_{JI} - \delta_{IJ} \left(\sum_M k_{IM} + k_{diss} + k_{CS} \delta_{I,RC} \right), \quad (3)$$

where k_{diss} and k_{CS} denote the dissipation and the RC charge separation rates, respectively; $\delta_{I,RC} = 1$ if the pigment cluster I belongs to a RC and $\delta_{I,RC} = 0$ otherwise. The rate matrix K has dimension N equal to the total number of pigment clusters in the network; these clusters involve the LH2, LH1 and RC pigments.

The quantum yield, q , of the chromatophore pigment network, defined as the probability of an absorbed photon to cause charge separation, can subsequently be expressed in terms of the matrix K in Eq. (3) [17, 23]

$$q = -k_{CS} \langle RC | K^{-1} | 0 \rangle, \quad (4)$$

where $|0\rangle$ denotes the N -dimensional vector of initial probabilities for the system and $|RC\rangle = \sum_I \delta_{I,RC} |I\rangle$. The quantum yield of $q=0.91$ determined thus for the vesicle shown in Fig. 7A is consistent with earlier studies [16, 17]. Following excitation transfer, the quinols that

are produced at the RC migrate to *cytbc*₁, which subsequently generates a proton-motive force to be utilized for ATP production at the ATP synthase.

In the following, the ATP turnover rate of the chromatophore under steady-state illumination is computed. This computation is achieved by relating the ATP production rate, $k_{ATP}(I)$, for a given illumination I to the quinol turnover in the chromatophore, which in turn is expressed in terms of the RC cycling time for quinones, $\tau_{RC}(I)$. The RC cycling time, $\tau_{RC}(I)$, is the mean time for the mobile quinone at the RC to be replaced upon conversion to quinol; $\tau_{RC}(I)$ depends on illumination and, through quinone diffusion dynamics, on the spatial arrangement of membrane proteins. The cycling time, $\tau_{RC}(I)$, acts as an important rate-determining constant of the system. It is currently prohibitive to simulate the quinone diffusion processes in the chromatophore directly. Therefore, the cycling time, $\tau_{RC}(I)$, is estimated from experimental observations [24]. Since spatial details and time dependence of quinone diffusion dynamics are not modelled, only steady state processes are considered below.

Bioenergetic processes other than ATP synthesis that utilize the proton-motive force, such as NADH/NADPH synthesis or motility, are not considered. Therefore, the cytoplasmic state of the cell is not modelled directly, and the cytoplasm is assumed to function as a perfect sink instead. Subsequently, the ATP turnover rates estimated in this study should be viewed as upper limits.

For typical low-light intensities accessible to purple bacteria, quinol turnover and subsequent ATP production are rate-limited primarily by processes in *cytbc*₁ as suggested also by other studies [25]. In the following, rate limitation at the ATP synthase is not considered explicitly since the reported maximal ATP turnover rate of 270 ± 40 ATP/s per ATP synthase [26] far exceeds ATP turnover achievable through photosynthetic quinol turnover processes even at saturation light intensities. Rate limitation due to the proton or cytochrome *c*₂ pools are also considered irrelevant for typical growth conditions as the respective processes become limiting only at very high light intensities or for vesicles containing a much greater number of *cytbc*₁ complexes than observed.

Detailed balance must hold for steady state illumination. Accordingly, the rate with which closed (i.e. unavailable for excitation processing) RCs open (i.e. become ready again for receiving an excitation to initiate quinone photochemistry) must equal the rate with which open RCs close. Therefore, follows

$$\frac{1}{\tau_{RC}(I)} (n_{RC} - n_{RC}^{open}(I)) = \frac{1}{2} I q p_{RC}(I), \quad (5)$$

where $1/\tau_{RC}(I)$ is the rate with which closed RCs reopen; n_{RC} and $n_{RC}^{open}(I)$ denote the total number of RCs in the system and those that are open, respectively; q is given by Eq. (4); $p_{RC}(I) = n_{RC}^{open}(I)/n_{RC}$ is the fraction of RCs that are open; the prefactor 1/2 accounts for each quinol turnover requiring two electrons; the light intensity I is given in terms of photons absorbed by the system per second.

The probability for open RCs, $p_{RC}(I)$, can be related to the cycling time, $\tau_{RC}(I)$, using eq. (5),

$$P_{RC}(I) = \left(1 + \frac{1}{2} I q \tau_{RC}(I) \frac{1}{n_{RC}}\right)^{-1}. \quad (6)$$

Since the cycling time, $\tau_{RC}(I)$, cannot be computed currently from a simulation of quinone diffusion processes, it is approximated below as an interpolation [27] between a low light limit, τ_L , and a high light limit, τ_H , determined experimentally. At the low light limit, where the quinone/quinol pool comprises almost entirely of quinones, a quinol departing the RC is replaced with a quinone from the immediate vicinity of the RC within time, τ_L , which is observed in low-light adapted LH2-rich chromatophores to be $\tau_L=3$ ms [24]. At the high light limit, where the pool comprises mostly of quinols, the replacement rate of quinones at the RC is limited by the total quinol processing rate, $B = n_B \tau_B^{-1}$, at the n_B *cytbc*₁ dimeric complexes of the chromatophore, τ_B denoting the quinol turnover time at a dimeric *cytbc*₁ complex. The high light limit of the cycling time, τ_H , can be determined by observing that the total quinol turnover rates at the RCs and *cytbc*₁ complexes must be equal for steady state illumination at large I , from which follows

$$\tau_H = \tau_B \frac{n_{RC}}{n_B}. \quad (7)$$

Occupancy of a *cytbc*₁ dimeric complex, $p_Q(I)$, i.e. the probability that it is involved in quinol turnover and is unavailable for further quinols, is given by

$p_Q(I) = 1 - \exp(-\frac{1}{2} I q / B)$; the rate Iq corresponds to the maximal electron turnover rate at the RCs and the factor 1/2 accounts for every quinol requiring two electron transfers. Accordingly, the interpolation of the cycling time, $\tau_{RC}(I)$, between the low and high illumination values, τ_L and τ_H , respectively, is given by the formula

$$\tau_{RC}(I) = \tau_L + (\tau_H - \tau_L) \left(1 - e^{-\frac{1}{2} I q B^{-1}}\right). \quad (8)$$

One can finally express the ATP turnover rate, $k_{ATP}(I)$, in terms of the illumination I and the utilization probability, $\eta_Q(I)$, for quinol turnover using eqs. (6)–(8)

$$k_{ATP}(I) = \frac{1}{2} I \eta_Q(I) = \frac{1}{2} I q \left(1 + \frac{1}{2} I q \tau_{RC}(I) \frac{1}{n_{RC}}\right)^{-1}, \quad (9)$$

where the prefactor 1/2 follows because the synthesis of one ATP requires the translocation of four protons and every electron cycled at a *cytbc*₁ dimeric complex translocates two protons. Here, the probability, $\eta_Q(I) = q p_{RC}(I)$, for an absorbed photon to be utilized for quinol turnover is the product of the probability for the photon to initiate charge transfer at a RC, namely q , given by eq. (4), and the probability for the RC to be open, $p_{RC}(I)$, given by eq. (6).

3. Results

3.1 Site-directed gold labelling of *cytbc*₁ complexes in intact chromatophores, and their detection by electron microscopy and AFM

A gene encoding the C-terminal His-tagged *cytbc*₁ was integrated into the *Rba. sphaeroides* genome, replacing the native *cytbc*₁ (*fbcC*) gene and ensuring a native copy number for the tagged protein. The resulting strain, BC1C10H bearing a His₁₀-tag on the cytoplasmic face of *cytbc*₁, grew photosynthetically at normal rates. Chromatophores were prepared from a photosynthetically grown culture of this strain were labelled with 5 nm Ni-NTA-gold beads in the absence of detergent, and fractionated on a sucrose step gradient as described in Materials and Methods. Controls with either no gold label or no His-tag were also analysed (Fig. 1) and only gold-labelled BC1C10H vesicles produced a new band at the 40–50% interface, with the original membrane band at the 20%–30% step almost absent. Labelled chromatophores from the 40–50% fraction were negatively stained and analysed by EM. The images (Fig. 2A–F) show that the majority of the *cytbc*₁ complexes (nanogold edge-to-edge separation 2.4 ± 0.5 nm (S.D.) $n=118$), occur as dimers in the membrane, consistent with the reported structure [7], and a recent kinetic study [28]. We used a nanogold concentration that minimised formation of vesicle clusters, which can be created by Ni-NTA groups on a gold bead interacting with His-tagged *cytbc*₁ complexes from different vesicles. Thus, only one half of a dimer might be labelled, giving apparent *cytbc*₁ monomers. Apparent monomers can also arise from one gold bead binding to both His-tags of the dimer, although the possibility of monomeric *cytbc*₁ complexes cannot be excluded. Another striking feature of these images is the tendency of *cytbc*₁ to form small clusters of two or more dimers.

The gold-labelled chromatophores harvested from the band at the 40–50% interface (Fig. 1, lane D) were also analysed by Peak Force Tapping AFM under liquid to attempt to identify protruding gold beads on the exposed cytoplasmic face of the chromatophore, as initially seen in EM (Fig. 2, 3A). In Fig. 3 we compare an EM image of labelled chromatophores with a possibly interlinked pair of chromatophores adsorbed to mica and imaged by AFM; interlinked vesicles have been seen in cryo-EM of frozen sectioned cells [29]. Fig. 3A shows the typical circular appearance of native chromatophores when dried down upon a carbon film EM grid; the diameter is greater than that of a chromatophore under liquid as these vesicles collapse upon desiccation, forming appressed discs [29]. In the AFM image of chromatophores under liquid in Fig. 3B the maroon-coloured extensions are protein-free lipid zones, as judged by their ~4 nm height above the mica substrate (also see Fig S1). The vesicles, which appear to be connected, are ~26 and ~30 nm high (see the section in Fig. S1A), similar to previous AFM measurements of isolated WT chromatophores of 37.6 ± 4.1 nm [19]; the smaller height here could indicate partial flattening of the chromatophores.

Discrete raised topology can be seen on the upper surfaces in Fig. 3B and one particular region of four similar height features is outlined by the red box on the right-hand vesicle. These paired, regular features give a low deformation signal (Fig. 3C, red box), in comparison with the white areas of the chromatophores where the AFM tip (the direction of the scan is shown by the white arrow) pushes into the vesicle side producing a high

deformation signal. These four topological features (Fig. 3C, red box) are tentatively assigned to NiNTA functionalised gold beads attached to *cytbc*₁ dimers. This cluster lies adjacent to the more closely spaced features denoted by pairs of coloured asterisks that are consistent with the 8–10 nm separation distance of RC H-subunits within a RC-LH1-PufX dimer [29]. These AFM images suggest that in these untreated native membrane vesicles of *Rba. sphaeroides* a group of dimeric *cytbc*₁ complexes sits adjacent to a short array of RC-LH1-PufX dimer complexes.

3.2 Detection of gold-labelled *cytbc*₁ complexes in membrane patches by electron microscopy and AFM

In order to gain a clearer picture of the distribution of *cytbc*₁ complexes, with respect to both RC-LH1-PufX and LH2 complexes, we labelled intact chromatophore membranes from the His₁₀-*cytbc*₁ mutant with NiNTA-nanogold, then opened them out using 0.1 mM β-DDM detergent and purified the resulting gold-labelled membrane patches on discontinuous sucrose gradients containing 0.025 mM TDM (see Materials and Methods). The EM images of the negatively stained gold-labelled patches (Fig. 4) confirmed the dimeric nature of *cytbc*₁ complexes and showed that several gold labels appear in a cluster; the larger cluster in Fig. 4F appears to be the sum of the *cytbc*₁ complexes from two chromatophores, which can be separately counted as five and nine gold labels. This is possibly a result of the tendency of the NiNTA gold beads to crosslink chromatophores by attaching to His-*cytbc*₁ complexes in initially separate vesicles. Thus, formation of flattened patches from crosslinked vesicles could effectively deplete the number of *cytbc*₁ complexes, as seen in the upper right patch of Fig 4E, and enhance others (Fig. 4A). Equally, such a membrane patch (Fig. 4A), representing a surface area greater than a single vesicle and with more RC-LH1-PufX, LH2 and *cytbc*₁ complexes, could have arisen from paired, interconnected vesicles; cryo-electron tomography of plunge-frozen *R. sphaeroides* cells [29] revealed interconnected vesicles, and it is likely that membrane patches prepared from such structures would resemble structures seen in Fig. 4A.

Nevertheless, we can use these patches to gain more information on the location of *cytbc*₁ complexes. Fig. 4A and B show the same patch; in Fig. 4A there are two regions of negatively stained larger features on either side of a larger region consisting of smaller circular features that we assign as LH2 complexes. The central membrane zone is clearly the largest, and we assign it to an LH2 domain; the other is RC-LH1-PufX. Our MS analyses indicate that these two complexes, together with *cytbc*₁, comprise 95% of the membrane proteins present so they also account for the majority of this membrane. Panel B displays a tentative assignment of LH2 complexes (green) and RC-LH1-PufX dimers (red/blue), based on the considerations above, in which gold-labelled *cytbc*₁ dimers form a cluster adjacent to both the densely-packed LH2 antenna domain and the RC-LH1-PufX dimer arrays. The membrane areas assigned for LH2:RC-LH1-PufX:*cytbc*₁, taking into account the known sizes of these complexes, are in the ratio 58:37:4. The molar ratios of these complexes were calculated from our proteomic and spectroscopic analyses and, also taking into account their known sizes, the membrane areas for LH2:RC-LH1-PufX:*cytbc*₁ are predicted to be 52:44:3. Finally, we counted the pixels in Fig. 4A, and the membrane areas (including lipids) assigned for LH2:RC-LH1-PufX:*cytbc*₁ are 66:25:9. It is interesting to note the agreement

between the first two ratios, and that the largest discrepancy between these two and the third ratio is for the region assigned to *cytbc*₁, suggesting lipid enrichment in these areas of membrane.

The regions adjoining gold-labelled *cytbc*₁ were also examined by AFM; the membrane patches are in direct contact with the mica substrate, unlike the upper membrane surface of intact vesicles, so it is possible to make more accurate estimates of the heights and deformation characteristics of the various complexes. Fig. 5A1 shows rows of RC-LH1-PufX dimers, delineated by white lines, and zig-zag areas of LH2 (green lines), which we compare with a typical non-labelled patch imaged to high resolution, Fig. 5B1. A section across the region of high topology (Fig. 5A1, magenta line) indicates a height of 15.6 nm, consistent with at least one gold nanobead attached to an underlying *cytbc*₁ complex; see the schematic representation in Fig. 5A2. The four scans prior to that shown in Fig. 5A are displayed in Fig. S2, and demonstrate that this topological feature survives the scanning process whereas a second, membrane-extrinsic feature arising from non-specifically bound surface protein is removed. The non-labelled patch (Fig. 5B2) showed no equivalent discrete high feature and consisted of a curved membranes composed largely of LH2 and RC-LH1-PufX regions. The simultaneously recorded deformation channel produces a clear, circular signal (Fig. 5A3), likely arising from the response of the AFM to lateral movement of the gold nanobead, which is connected to the C-terminus of *cytbc*₁ by a flexible 20-residue linker. Interaction of the scanning AFM probe with peripheral regions of the gold bead and consequent displacement of the bead gives a circular, high deformation signal. In the central region the deformation signal is similar to that of the surrounding protein, consistent with the AFM tip depressing directly down on the nanobead, thus compressing the underlying *cytbc*₁, as illustrated in the associated cartoon (Fig. 5A3). The position of this central region corresponds to the 15.6 nm topological feature in Fig. 5A1, supporting its assignment as a gold-labelled *cytbc*₁ complex.

The feature assigned to the *cytbc*₁ complex in Fig. 5A1 & A3 lies adjacent to a region consisting of LH2 complexes and to an array of paired topological features outlined in white (Fig. 5A1). A section across one of these pairs (Fig. 5A1, blue line, Fig. 5A5) shows a separation of 8.3 nm, consistent with the RC-RC distance measured from the structural model of the dimeric RC-LH1-PufX complex (Fig. 5A2), and with previous AFM data on this membrane-bound complex [29]. Sections across seven of these pairs (Fig. S3) show that they are separated by 7.5 ± 0.8 nm, as reported earlier for core dimers appressed to the mica surface [29], indicating that this region of the membrane adjacent to the gold bead consists of dimeric RC-LH1-PufX complexes. The low resolution and tip convolution effects do not allow us to assess the distances between the surrounding complexes and the *cytbc*₁. The higher resolution image of the unlabeled membrane (Fig. 5B1) allows the unambiguous assignment of the LH2 region and arrays of dimeric RC-LH1-PufX complexes; additionally the image shows a monomeric core complex immediately adjacent to one row of core dimers. The two core complex arrays surround a zone of limited topology (Fig. 5B4 & 5), which indicates the presence of additional membrane proteins. This region of the membrane is modelled in Fig 5B2 & 3, shown in side and top views, respectively, using measurements taken from the data in Fig. 5B1, together with the crystal structures of the *Rba. sphaeroides*

*cytbc*₁ complex (2QJP) and the core dimer [30]. The model shows that two *cytbc*₁ complexes can be readily accommodated between the two rows of dimers, and the sections (Fig. 5B4 & B5) demonstrate that the heights measured from the mica to the cytoplasmic surface of the unknown proteins are consistent with the presence of *cytbc*₁ complexes, probably not fully in contact with the mica substrate. Thus the AFM data on membrane patches are consistent with the EM images in Fig. 4, and with the AFM images of intact untreated chromatophores, Fig. 3A–E, showing that *cytbc*₁ complexes are found adjacent to RC-LH1-PufX dimer arrays.

3.3 Retrieval of co-purifying complexes using the His-tagged *cytbc*₁ AFM of a gold-labelled membrane

We sought biochemical evidence for associations between *cytbc*₁ and RC-LH1-PufX complexes; chromatophore vesicles were partially solubilised by gentle detergent treatment with a range of β -dodecyl maltoside (β -DDM) concentrations, then Ni-NTA affinity chromatography was used to retrieve His-tagged *cytbc*₁ together with any associated complexes. Increasing concentrations of β -DDM (0.1, 0.5, 1.0, 2.0 and 2.5%) progressively stripped proteins, lipids and quinones from the immediate environment of His-*cytbc*₁, thereby probing the environment around this complex. The composition of the *cytbc*₁ pull-down at each initial β -DDM concentration is displayed in Table 2, expressed as moles of each component per mole of eluted *cytbc*₁ dimer. Absorption spectra of each pull-down are displayed in Fig. S4. The levels of protein complexes in the starting chromatophore vesicles were quantified by mass spectrometry; lipids and quinones were quantified following extraction as detailed in the Methods section. The data in Table 2 and in Fig. 6 show that even at the lowest detergent concentration approximately 90% of proteins, lipids and quinones had been removed from the environment of the *cytbc*₁. This points to an unusually detergent-susceptible environment around the *cytbc*₁. As the solubilising detergent concentration increases there is a tendency for the remaining RC-LH1-PufX complexes to co-purify with *cytbc*₁, whereas a greater proportion of the LH2 complexes become detached.

3.4. Quantitation of the major membrane protein complexes in chromatophore membranes

In order to build a quantitative structural model of a chromatophore vesicle we used mass spectrometry (MS) to count the number of RC, *cytbc*₁, ATP synthase, *cytaa*₃ and *cytcb*₃ membrane protein complexes. For this quantitative MS analysis an ¹⁵N-labelled internal standard was constructed as an artificial protein composed of concatenated tryptic peptide sequences [13, 14] overproduced in *E. coli* and purified on a Ni²⁺-charged chelating Sepharose column. Chromatophores were mixed with ¹⁵N-labelled artificial protein standard and, following digestion, tryptic peptides were analysed in duplicate by nanoflow liquid chromatography coupled to a Maxis UHR-TOF mass spectrometer.

*Cytbc*₁ complexes were quantified using tryptic peptides from the FbcC (*cyt*_{c1}) and FbcF (Rieske) proteins; ATP synthase was quantified by its membrane-anchored peripheral stalk subunits AtpF (b) and AtpX (b') which are present at one copy each per complex [31]. The α -subunit (AtpA), residing in the membrane-extrinsic F₁ sector, occurs in a stoichiometry of 3 per complex [30]. Our observation of a stoichiometry of 4–5 AtpA per chromatophore instead of the 6 expected for two ATP synthases highlights the partial loss of F₁ during

chromatophore isolation and demonstrates an advantage, in this case, of using an MS-based determination of the stoichiometry of membrane-anchored proteins over a functional assay. The *aa₃* and *cbb₃* terminal *cytc* oxidases were quantified by their CoxII and CcoO subunits, respectively. The former was found to be absent from chromatophores while the *cbb₃* *cytc* oxidase was detected at a copy number of 1. This expression pattern is as expected, given the anaerobic culture conditions used in this study [32]. These results (Table 1) indicate a *cytbc₁*:RC stoichiometry of 0.28–0.36, equivalent to 3–4 *cytbc₁* dimers in a chromatophore containing 24 RCs (see Fig. 7). The ATP synthase has a stoichiometry of 0.08–0.09, relative to the RC, equivalent to 2 complexes per chromatophore.

3.5 Integration of light-harvesting function in a chromatophore vesicle based on an atomic-level structural model

The model of a photosynthetic membrane vesicle combines earlier AFM [6, 19], EM [33–35], crystallography [36] and spectroscopy [37] data with the current MS (Table 1), EM and AFM data (Figs. 2–5). This vesicle, adapted from a prior model [17, 16], has an inner diameter of 50 nm and features a ‘low light’ LH2:RC stoichiometry of 2.7, as well as a packing pattern of LH2 complexes consistent with previous AFM data [19]. Some of the core complexes are monomers, in keeping with biochemical and AFM analyses of photosynthetic membranes [6, 38–40]. Fig. 7A displays the model, which comprises the major components of bacterial photosynthesis. Given the delocalisation of proton gradients in the membrane lumen, the exact position of the ATPase is not critical for its function or for our model. The locations of the ATP synthase complexes are assigned tentatively based upon the expectation that they would tend to partition amongst the LH2 complexes, which are of a similar size and shape to the membrane bound F₀ rotor, a cylinder 6 nm tall and 6.2 nm wide [41]. Furthermore, proteomics data suggest a preferential colocalization of ATP synthase and LH2 complexes [21]. The four dimeric *cytbc₁* complexes are grouped as (2-1-1), giving a RC: *cytbc₁* ratio of 3:1, compatible with the quantitative MS analysis (Tables 1 and S1). Extraction data (Table 2) show that such a vesicle would contain ~500–900 quinones, of which 240–360 are sequestered within the dimeric RC-LH1-PufX complexes [11]. A pool of quinones is likely to be closely associated with the immediate environment around core dimers and also around the *cytbc₁* complexes, providing a buffer against rapid fluctuations of light intensity, and ensuring robustness of cyclic electron transfer. Associations of two or more RC-LH1-PufX dimers could provide channels for short-range Q/QH₂ quinone diffusion between RC Q_B sites and *cytbc₁* complexes [30], contributing to the driving force for the forward reactions in the *cytbc₁* catalytic cycle [42].

The primary function of the chromatophore is to capture, transfer, and convert solar energy for ATP production. We used the atomic-level model shown in Fig. 7 to simulate the interconnected energy, electron and proton transfer processes in a chromatophore vesicle (see Material and methods). For the purposes of this study we assumed that cytochrome *c₂* diffusion and ATP/ADP conversion are not rate-limiting sub-processes. A comparison of the turnover rates of constituent proteins indicates that *cytbc₁* complexes are rate-determining components at almost all illuminations. To test this assumption we consider a control vesicle containing only one *cytbc₁* dimer complex, with 7 additional LH2 complexes compensating for the surface area of the 3 *cytbc₁* complexes removed from the model shown in Fig. 7A.

Fig. 7B, dashed line, shows that this control vesicle containing only one *cytbc*₁ dimer can only achieve 37% of the steady-state ATP production rate at a typical low light intensity of 3% full sunlight, compared to a vesicle with 4 *cytbc*₁ dimers (Fig. 7B, solid line). For the vesicle shown in Fig. 7A the ATP turnover rate is 84–119 ATP/s for light intensities of 10–30 W/m² (typical illumination conditions). Such low light conditions (~3% or less of bright sunlight) almost saturate the energy conversion mechanism of the chromatophore; at full sunlight (1 kW/m²) ATP turnover increases only to 158 ATP/s. Thus, the chromatophore achieves half-maximal ATP turnover already at around 1% of full sunlight, indicating optimal adaptation for low light intensities.

4. Discussion

By using negative stain EM, high resolution AFM, affinity chromatography and quantitative MS we have established the membrane environment and the typical stoichiometries of the *cytbc*₁ complex in chromatophores of *Rba. sphaeroides* with respect to the RC-LH1-PufX and LH2 complexes and also the ATP synthase. Identification of *cytbc*₁ required genomic integration of the modified *fbcC* gene, replacing the native gene, to introduce a His₁₀-tag onto the C-terminus of *cytbc*₁. Gold labeling of the tagged complex provided the topology normally absent from the cytoplasmic face of this *cytbc*₁ complex, and the means to find this complex using AFM. The electron-dense gold label also facilitated identification of *cytbc*₁ by EM. The EM and AFM data are consistent with *cytbc*₁ complexes positioned adjacent to RC-LH1-PufX complexes.

Pulldown experiments on chromatophore membranes with His-tagged *cytbc*₁ as bait (Table 2 and Fig. 6) showed that approximately 90% of the chromatophore protein, lipids and quinones are removed by the lowest concentration (0.1%) of β -DDM detergent. This detergent-susceptible environment could arise from an enrichment of lipids and quinones round the His-*cytbc*₁ complexes; RC-LH1-PufX complexes sequester up to half the chromatophore quinones (Table 2 and [5, 11]), implying quinone enrichment of the local *cytbc*₁-RC-LH1-PufX membrane environment under steady state illumination conditions as these mobile carriers cycle between the complexes. A quinone-rich phase was proposed to surround the RC-LH1-PufX complexes, on the basis of kinetic data [5]. Approximately 10% of the original RC-LH1-PufX complexes retain an association with His-*cytbc*₁, even in the presence of 2.5% β -DDM, implying a weak but non-stoichiometric interaction between these complexes, rather than a ‘hardwired’ *cytbc*₁-RC-LH1-PufX supercomplex of fixed stoichiometry. The small electron transfer domains proposed earlier for *Rba. sphaeroides* [43], are likely to exist, but not as fixed RC-LH1-PufX-*cytbc*₁ supercomplexes. Instead, *cytbc*₁ complexes sit adjacent to RC-LH1-PufX complexes in disordered areas likely caused by the packing mismatch between LH2 and core complexes, with the majority of the RC-LH1-PufX complexes not in direct contact with *cytbc*₁.

This arrangement might appear to hinder the quinones as they shuttle rapidly between nonadjacent RC-LH1-PufX and *cytbc*₁ complexes, but the recent structural study of the *Rba. sphaeroides* RC-LH1-PufX complex [30] proposes a channel for quinones to migrate along rows of core dimers. Moreover, imperfect packing of LH2 complexes round the RC-LH1-PufX complexes (see Fig. 7) could create the space for quinone migration along the external

faces of RC-LH1-PufX complexes. The dimer structure identified a gap in the LH1 ring adjacent to PufX that allows exchange of quinones and quinols through the LH1 barrier. This work also identified a cavity within the LH1 ring, close to the RC Q_B site [30]. Finally, the structure raised the possibility that quinones can migrate between the two halves of the RC-LH1-PufX dimer, consistent with kinetic data demonstrating quinone sharing by the two RCs within a dimer [5]. These three structural features of the complex could allow rows of core dimers to form channels for quinone diffusion to a nearby *cytbc*₁ complex. Such an arrangement is depicted in Fig. 7, where three of the *cytbc*₁ dimers are positioned at the end of two rows of three RC-LH1-PufX complexes. Thus, even ‘remote’ RC-LH1-PufX dimers are in communication with two or more *cytbc*₁. Crofts [44] pointed out that, rather than a particular RC having sole access to a dedicated *cytbc*₁ within a supercomplex, quinols or cytochrome *c*₂ can visit several *cytbc*₁ complexes, and this seems likely on the basis of our EM and AFM data.

Another possible consequence of the proximity of *cytbc*₁ and RC-LH1-PufX complexes is an effective confinement of the extrinsic mobile electron carrier cytochrome *c*₂, which, as discussed in [1], also must cycle between these complexes to fill the electron hole created by RC photochemistry and enable repeated turnovers of the *cytbc*₁ complex. In *Rba. sphaeroides* this confinement within the chromatophore interior is enhanced by the tight curvature of the chromatophore vesicle which, if it encloses perhaps 12 cytochrome *c*₂ molecules, results in a cytochrome *c*₂ concentration of 0.6 mM. The distances over the internal vesicle surface for diffusion of cytochrome *c*₂ between the RC and *cytbc*₁ are in the 10–30 nm range, apparently sufficient for cyclic electron transfer.

Although LH2 complexes do not bind or sequester quinone [11], AFM mapping of membranes from an LH2-only mutant of *Rba. sphaeroides* showed that LH2 packing could allow percolation of quinones. There are as many 500 quinones in a chromatophore that are not sequestered by the RC-LH1-PufX complexes; although some of them contribute to a quinone- and lipid-rich phase surrounding the RC-LH1-PufX and *cytbc*₁ complexes [5] it is possible that the remainder form a more slowly diffusible pool that equilibrates over the whole vesicle on timescales longer than the 1–2 ms required for cyclic electron flow, thus providing a secondary buffer. Such a ‘slow’ quinone pool could also be important for the function of other complexes such as the cytochrome *cbb*₃ oxidase, which we found at a level one per chromatophore (Table 1), but currently we have no information on the membrane location of respiratory chain components

The chromatophore vesicle represents a membrane surface area of ~7500 nm² that apparently partitions to some degree into zones for solar energy collection (LH2), photochemistry (RC-LH1-PufX) and secondary electron transfer (*cytbc*₁). Thus light-driven cyclic electron flow appears primarily to be sustained by short-range diffusion between *cytbc*₁ and RC-LH1-PufX complexes, rather than random migration of quinones over the whole chromatophore vesicle. Our proposal parallels the organisation of the equivalent membrane complexes in stacked plant thylakoid membranes, where kinetic studies showed that plastoquinone diffusion between Photosystem II and dimeric *cytb₆f* complexes is confined within small membrane domains [45], as proposed earlier [43]. With regard to supercomplexes in oxygen-evolving photosynthesising organisms, *cytb₆f* complexes

associate with Photosystem I under conditions that favour cyclic electron flow in *Chlamydomonas* [46, 47].

Kinetic models of the chromatophore that account for the interlinked processes of light absorption, energy transfer, electron flow, generation of a protonmotive force and ATP synthesis have been formulated before [25, 48]. In this study, we have updated our existing structural model of the chromatophore vesicle [16, 17] to take into account the new information on the stoichiometries of the major membrane components and their locations obtained using EM, AFM and MS. We constructed an *in silico* model chromatophore to test the efficiency of this self-contained energy transduction vesicle to produce ATP as a function of illumination. The model clearly demonstrates a robust system that is optimized for the production of ATP under low light illumination, the expected growth conditions for the purple phototrophs such as *Rba. sphaeroides* in a stratified lake. The chromatophore architecture presented above in Fig. 7A, particularly the observed number and organization of *cytbc*₁ complexes, optimizes photosynthetic function at low and fluctuating light intensities. The conversion of absorbed energy to ATP appears to be determined by the number of *cytbc*₁ complexes, as seen in Fig. 7B; *cytbc*₁ was also identified as the ‘kinetic bottleneck’ in [25]. We propose that quinone-enriched zones in proximity to the *cytbc*₁ complexes and the RC Q_B site [11, 30, 33, 34] act as kinetic buffers that smooth the effects of fluctuating light (at sub-second timescales), allowing continuous ATP production during intermittent dark periods. This supramolecular arrangement ensures that quinone diffusion is not rate limiting [5, 49]. Therefore, the photosynthetic apparatus displays *robustness* (against rapid fluctuations in light intensity) and *optimality* (of composition for typical growth conditions), thus illustrating adaptiveness, not only at the level of individual proteins as reported earlier [50, 51] but also at a system level integration of function.

Supplementary Material

Refer to Web version on PubMed Central for supplementary material.

Acknowledgments

M.L.C. and G.J.L. were supported by funding from the Engineering and Physical Sciences Research Council (EPSRC, Grant EP/I012060/1), UK. P.Q., P.J.J., A.A.B. J.D.O., M.J.D., and C.N.H. gratefully acknowledge funding from the Biotechnology and Biological Sciences Research Council (U.K.). This work was also supported as part of the Photosynthetic Antenna Research Center (PARC), an Energy Frontier Research Center funded by the US Department of Energy, Office of Science, and Office of Basic Energy Sciences under Award Number DE-SC0001035. PARC’s role was to partially fund the Multimode VIII AFM system and to provide partial support for C.N.H. and A.A.B. M.S. and K.S. were supported by the National Science Foundation (MCB-1157615 and PHY0822613) and the National Institutes of Health (9P41GM104601). The authors would like to thank Dr Cvetelin Vasilev, Professor Per Bullough, Elizabeth Martin and David Mothersole for helpful advice.

Abbreviations

AFM	atomic force microscopy
BChl(s)	bacteriochlorophyll(s)
R.	Rhodobacter

LH	light-harvesting
PFT	PeakForce Tapping (AFM)
RC	Reaction Centre
TEM	transmission electron microscopy
TM	Tapping Mode (AFM)
NiNTA	nickel triacetic acid
His	Histidine
β-DDM	β -dodecyl maltoside
TDM	n-tetradecyl- β -D-maltopyranoside

References

1. Lavergne, J.; Verméglio, A.; Joliot, P. Functional coupling between reaction centers and cytochrome *bc*₁ complexes. In: Hunter, CN.; Daldal, F.; Thurnauer, MC.; Beatty, JT., editors. *The Purple Phototrophic Bacteria*. Netherlands, Dordrecht: Springer; 2008. p. 509-536.
2. Joliot P, Verméglio A, Joliot A. Evidence for supercomplexes between reaction centers, cytochrome *c*₂ and cytochrome *bc*₁ complex in *Rhodobacter sphaeroides* whole cells. *Biochim. et Biophys. Acta*. 1989; 975:336–345.
3. Crofts A, Guergova-Kuras M, Hong SJ. Chromatophore heterogeneity explains phenomena seen in *Rhodobacter sphaeroides* previously attributed to supercomplexes. *Photosyn. Res*. 1998; 55:357–362.
4. Rich PR. Electron and proton transfers through quinones and cytochrome *bc* complexes. *Biochim. Biophys. Acta*. 1984; 768:53–79. [PubMed: 6322844]
5. Comayras R, Jungas C, Lavergne J. Functional consequences of the organization of the photosynthetic apparatus in *Rhodobacter sphaeroides* - I. Quinone domains and excitation transfer in chromatophores and reaction center center antenna complexes. *J. Biol. Chem*. 2005; 280:11203–11213. [PubMed: 15632164]
6. Bahatyrova S, Frese RN, Siebert CA, Olsen JD, van der Werf KO, van Grondelle R, Niederman RA, Bullough PA, Otto C, Hunter CN. The native architecture of a photosynthetic membrane. *Nature*. 2004; 430:1058–1062. [PubMed: 15329728]
7. Esser L, Elberry M, Zhou F, Yu C-A, Yu L, Xia D. Inhibitor-complexed structures of the cytochrome *bc*₁ from the photosynthetic bacterium *Rhodobacter sphaeroides*. *J. Biol. Chem*. 2007; 283:2846–2857. [PubMed: 18039651]
8. Simon R, Priefer U, Pühler A. A broad host range mobilization system for *in vivo* genetic engineering: transposon mutagenesis in gram negative bacteria. *Bio/Technology*. 1983; 1:784–791.
9. Roh JH, Kaplan S. Genetic and phenotypic analyses of the *rdx* locus of *Rhodobacter sphaeroides* 2.4.1 [In Process Citation]. *J. Bacteriol*. 2000; 182:3475–3481. [PubMed: 10852880]
10. Rouser G, Fleischer S, Yamamoto A. 2-dimensional thin layer chromatographic separation of polar lipids and determination of phospholipids by phosphorus analysis of spots. *Lipids*. 1970; 5:494–496. [PubMed: 5483450]
11. Dezi M, Francia F, Mallardi A, Colafemmina G, Palazzo G, Venturoli G. Stabilization of charge separation and cardiolipin confinement in antenna-reaction center complexes purified from *Rhodobacter sphaeroides*. *Biochimica et Biophysica Acta*. 2007; 1767:1041–1056. [PubMed: 17588528]
12. Wang H, Wang F, Wei Z, Hu H. Quinone profiles of microbial communities in sediments of Haihe River–Bohai Bay as influenced by heavy metals and environmental factors. *Environmental Monitoring and Assessment*. 2011; 176:157–167. [PubMed: 20568008]

13. Pratt JM, Simpson DM, Doherty MK, Rivers J, Gaskell SJ, Beynon RJ. Multiplexed absolute quantification for proteomics using concatenated signature peptides encoded by QconCAT genes. *Nat. Protoc.* 2006; 1:1029–1043. [PubMed: 17406340]
14. Rivers J, Simpson DM, Robertson DH, Gaskell SJ, Beynon RJ. Absolute multiplexed quantitative analysis of protein expression during muscle development using QconCAT. *Mol Cell Proteomics.* 2007; 6:1416–1427. [PubMed: 17510050]
15. Finehout EJ, Cantor JR, Lee KH. Kinetic characterization of sequencing grade modified trypsin. *Proteomics.* 2005; 5:2319–2321. [PubMed: 15880790]
16. Sener MK, Olsen JD, Hunter CN, Schulten K. Atomic-level structural and functional model of a bacterial photosynthetic membrane vesicle. *Proc. Natl. Acad. Sci. USA.* 2007; 104:15723–15728. [PubMed: 17895378]
17. Sener M, Strümpfer J, Timney JA, Freiberg A, Hunter CN, Schulten K. Photosynthetic vesicle architecture and constraints on efficient energy harvesting. *Biophys J.* 2010; 99:67–75. [PubMed: 20655834]
18. Adams PG, Hunter CN. Adaptation of intracytoplasmic membranes to altered light intensity in *Rhodobacter sphaeroides*. *Biochim. Biophys Acta.* 2012; 1817:1616–1627. [PubMed: 22659614]
19. Olsen JD, Tucker JD, Timney JA, Qian P, Vassilev C, Hunter CN. The organization of LH2 complexes in membranes from *Rhodobacter sphaeroides*. *J. Biol. Chem.* 2008; 283:30772–30779. [PubMed: 18723509]
20. Hsin J, Strümpfer J, Sener M, Qian P, Hunter CN, Schulten K. Energy transfer dynamics in an RC–LH1–PufX tubular photosynthetic membrane. *New J Phys.* 2010; 12:085005–085005.
21. Woronowicz K, Niederman RA. Proteomic analysis of the developing intracytoplasmic membrane in *Rhodobacter sphaeroides* during adaptation to low light intensity. *Adv. Exp. Med. Biol.* 2010; 675:161–178. [PubMed: 20532741]
22. Strümpfer J, Sener M, Schulten K. How quantum coherence assists photosynthetic light harvesting. *J. Phys. Chem. Lett.* 2012; 3:536–542. [PubMed: 22844553]
23. Sener MK, Strümpfer J, Hsin J, Chandler D, Scheuring S, Hunter CN, Schulten K. Förster energy transfer theory as reflected in the structures of photosynthetic light-harvesting systems. *Chem. Phys. Chem.* 2011; 12:518–531. [PubMed: 21344591]
24. Woronowicz K, Sha D, Frese RN, Niederman RA. The accumulation of the light-harvesting 2 complex during remodeling of the *Rhodobacter sphaeroides* intracytoplasmic membrane results in a slowing of the electron transfer turnover rate of photochemical reaction centers. *Biochemistry.* 2011; 50:4819–4829. [PubMed: 21366273]
25. Geyer T, Helms V. Reconstruction of a kinetic model of the chromatophore vesicles from *Rhodobacter sphaeroides*. *Biophysical Journal.* 2006; 91:927–937. [PubMed: 16714340]
26. Etzold C, Deckers-Hebestreit G, Altendorf K. Turnover number of *Escherichia coli* F₀F₁ ATP synthase for ATP synthesis in membrane vesicles. *Eur. J Biochem.* 1997; 243:336–343. [PubMed: 9030757]
27. Mauzerall D. The optical cross section and absolute size of a photosynthetic unit. *Photosynth. Res.* 1986; 10:163–170. [PubMed: 24435361]
28. wierzchek M, Cieluch E, Sarewicz M, Borek A, Moser CC, Dutton PL, Osyczka A. An electronic bus bar lies in the core of cytochrome *bc*₁. *Science.* 2010; 329:451–454. [PubMed: 20651150]
29. Tucker JD, Siebert CA, Escalante M, Adams PG, Olsen JD, Otto C, Stokes DL, Hunter CN. Membrane invagination in *Rhodobacter sphaeroides* is initiated at curved regions of the cytoplasmic membrane, then forms both budded and fully detached spherical vesicles. *Mol Microbiol.* 2010; 76:833–847. [PubMed: 20444085]
30. Qian P, Papiz MZ, Jackson PJ, Brindley AA, Ng IW, Olsen JD, Dickman MJ, Bullough PA, Hunter CN. The 3-D structure of the *Rhodobacter sphaeroides* RC-LH1–PufX complex: dimerization and quinone channels promoted by PufX. *Biochemistry.* 2013; 52:7575–7585. [PubMed: 24131108]
31. von Ballmoos C, Wiedenmann A, Dimroth P. Essentials for ATP synthesis by F₁F₀ ATP synthases. *Annu. Rev. Biochem.* 2009; 78:649–672. [PubMed: 19489730]

32. Mouncey NJ, Kaplan S. Oxygen regulation of the *ccoN* gene encoding a component of the *ccb₃* oxidase in *Rhodobactersphaeroides* 2.4.1^T: involvement of the FnrL protein. *J Bacteriol.* 1998; 180:2228–2231. [PubMed: 9555909]
33. Qian P, Hunter CN, Bullough PA. The 8.5 Å projection structure of the core RC-LH1-PufX dimer of *Rhodobacter sphaeroides*. *J. Mol. Biol.* 2005; 349:948–960. [PubMed: 15907932]
34. Qian P, Bullough P, Hunter CN. Three-dimensional reconstruction of a membrane-bending complex. *J. Biol. Chem.* 2008; 283:14002–14011. [PubMed: 18326046]
35. Walz T, Jamieson SJ, Bowers CM, Bullough PA, Hunter CN. Projection structures of three photosynthetic complexes from *Rhodobacter sphaeroides*: LH2 at 6 Å, LH1 and RC-LH1 at 25 Å. *J. Mol. Biol.* 1998; 282:833–845. [PubMed: 9743630]
36. McDermott G, Prince SM, Freer AA, Hawthornthwaite-Lawless AM, Papiz MZ, Cogdell RJ, Isaacs NW. Crystal structure of an integral membrane light-harvesting complex from photosynthetic bacteria. *Nature.* 1995; 374:517–521.
37. Frese RN, Siebert CA, Niederman RA, Hunter CN, Otto C, van Grondelle R. The long-range organization of a native photosynthetic membrane. *Proceedings of the National Academy of Sciences.* 2004; 101:17994–17999.
38. Francia F, Wang J, Zischka H, Venturoli G, Oesterhelt D. Role of the N- and C-terminal regions of the PufX protein in the structural organization of the photosynthetic core complex of *Rhodobacter sphaeroides*. *Eur J Biochem.* 2002; 269:1877–1885. [PubMed: 11952789]
39. Ratcliffe EC, Tunnicliffe RB, Ng IW, Adams PG, Qian P, Holden-Dye K, Jones MR, Williamson MP, Hunter CN. Experimental evidence that the membrane-spanning helix of PufX adopts a bent conformation that facilitates dimerisation of the *Rhodobacter sphaeroides* RC-LH1 complex through N-terminal interactions. *Biochim. Biophys. Acta.* 2011; 1807:95–107. [PubMed: 20937243]
40. Ng IW, Adams PG, Mothersole DJ, Vasilev C, Martin EC, Lang HP, Tucker JD, Hunter CN. Carotenoids are essential for normal levels of dimerisation of the RC-LH1-PufX core complex of *Rhodobacter sphaeroides*: characterisation of R-26 as a *crtB*(phytoene synthase) mutant. *Biochim. Biophys. Acta.* 2011; 1807:1056–1063. [PubMed: 21651888]
41. Saroussi S, Schushan M, Ben-Tal N, Junge W, Nelson N. Structure and flexibility of the C-ring in the electromotor of rotary F₀-F₁-ATPase of pea chloroplasts. *PLoS ONE.* 2012; 7(9):e43045. [PubMed: 23049735]
42. Osyczka A, Moser CC, Daldal F, Dutton PL. Reversible redox energy coupling in electron transfer chains. *Nature.* 2004; 427:607–612. [PubMed: 14961113]
43. Lavergne J, Joliot P. Restricted diffusion in photosynthetic membranes. *Trends Biochem Sci.* 1991; 16:129–134. [PubMed: 1877087]
44. Crofts AR, Guergova-Kuras M, Hong S. Chromatophore heterogeneity explains phenomena seen in *Rhodobacter sphaeroides* previously attributed to supercomplexes. *Photosynthesis Research.* 1998; 55:357–362.
45. Kirchhoff H, Horstmann S, Weis E. Control of the photosynthetic electron transport by PQ diffusion microdomains in thylakoids of higher plants. *Biochim. Biophys. Acta.* 2000; 1459:148–168. [PubMed: 10924908]
46. Iwai M, Takizawa K, Tokutsu R, Okamuro A, Takahashi Y, Minagawa J. Isolation of the elusive supercomplex that drives cyclic electron flow in photosynthesis. *Nature.* 2010; 464:1210–1213. [PubMed: 20364124]
47. Takahashi H, Clowez S, Wollman F-A, Vallon O, Rappaport F. Cyclic electron flow is redox-controlled but independent of state transition. *Nature Communications.* 2013; 4:1–8.
48. Caycedo-Soler F, Rodriguez FJ, Quiroga L, Johnson NF. Light-harvesting mechanism of bacteria exploits a critical interplay between the dynamics of transport and trapping. *Phys. Rev. Lett.* 2010; 104:158302. [PubMed: 20482023]
49. Kirchhoff H, Mukherjee U, Galla HJ. Molecular architecture of the thylakoid membrane: lipid diffusion space for plastoquinone. *Biochemistry.* 2002; 41:4872–4882. [PubMed: 11939782]
50. Sener MK, Lu D, Ritz T, Park P, Fromme P, Schulten K. Robustness and optimality of light harvesting in cyanobacterial Photosystem I. *J. Phys. Chem. B.* 2013; 106:7948–7960.

51. Noy D, Moser CC, Dutton PL. Design and engineering of photosynthetic light-harvesting and electron transfer using length, time, and energy scales. *Biochimica et Biophysica Acta*. 2006; 1757:90–105. [PubMed: 16457774]

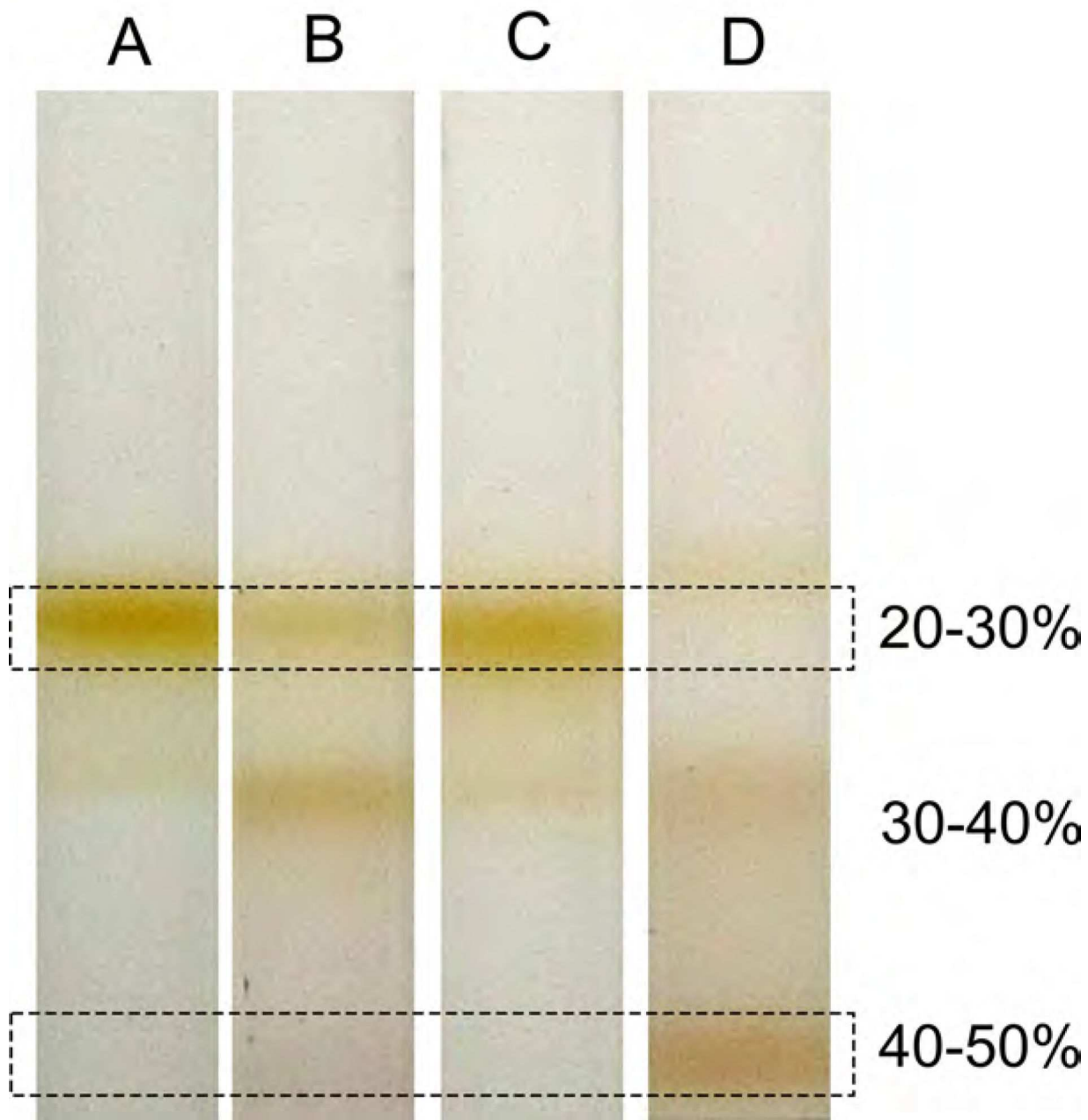


Fig. 1. Isolation of gold-labelled ICM vesicles on sucrose density gradients

Vesicles were treated with Ni-NTA-Nanogold® then fractionated on a 20%/30%/40%/50% (w/w) sucrose step gradient. A. Unlabelled wild-type vesicles at the 20–30% interface (upper box). B. wild-type vesicles labelled with Ni-NTA-Nanogold®. The vesicles migrate lower in the gradient due to unspecific gold labelling; the colouration at the 30–40% interface reflects the optical properties of the gold beads. C. Unlabelled His-cyt bc_1 (strain BC1C10H) vesicles, D. BC1C10H vesicles labelled with Ni-NTA-Nanogold®; as a result of labelling the original membrane band is almost absent. The band at the 30–40% interface

consists of partially-labelled vesicles. The lower box highlights the location of the specifically-labelled vesicles at the 40–50% interface. The gold beads confer a pink hue to the membranes.

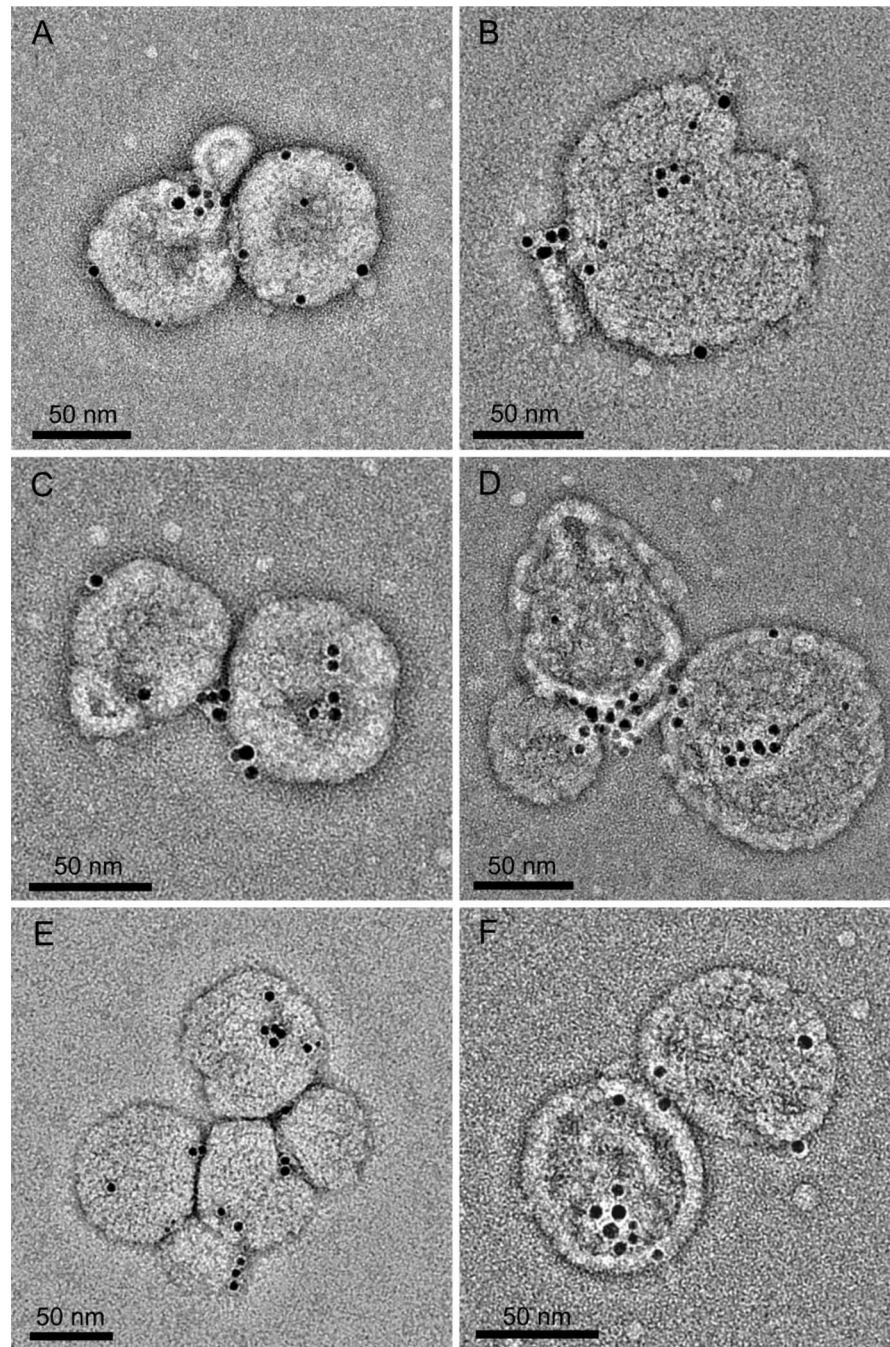


Figure 2. Identification and membrane localisation of *cytb*₁ complexes

A–F. Negatively stained whole chromatophores with *cytb*₁ complexes labelled with gold NTA-Nanogold[®]. The edge-to-edge separation of pairs of gold beads is 2.4 ± 0.5 (S.D.) nm $n=118$, compatible with the structure of the *Rba. sphaeroides* *cytb*₁ dimer complex^{12,13} and also the surface shell of the Ni-NTA nanoparticle.

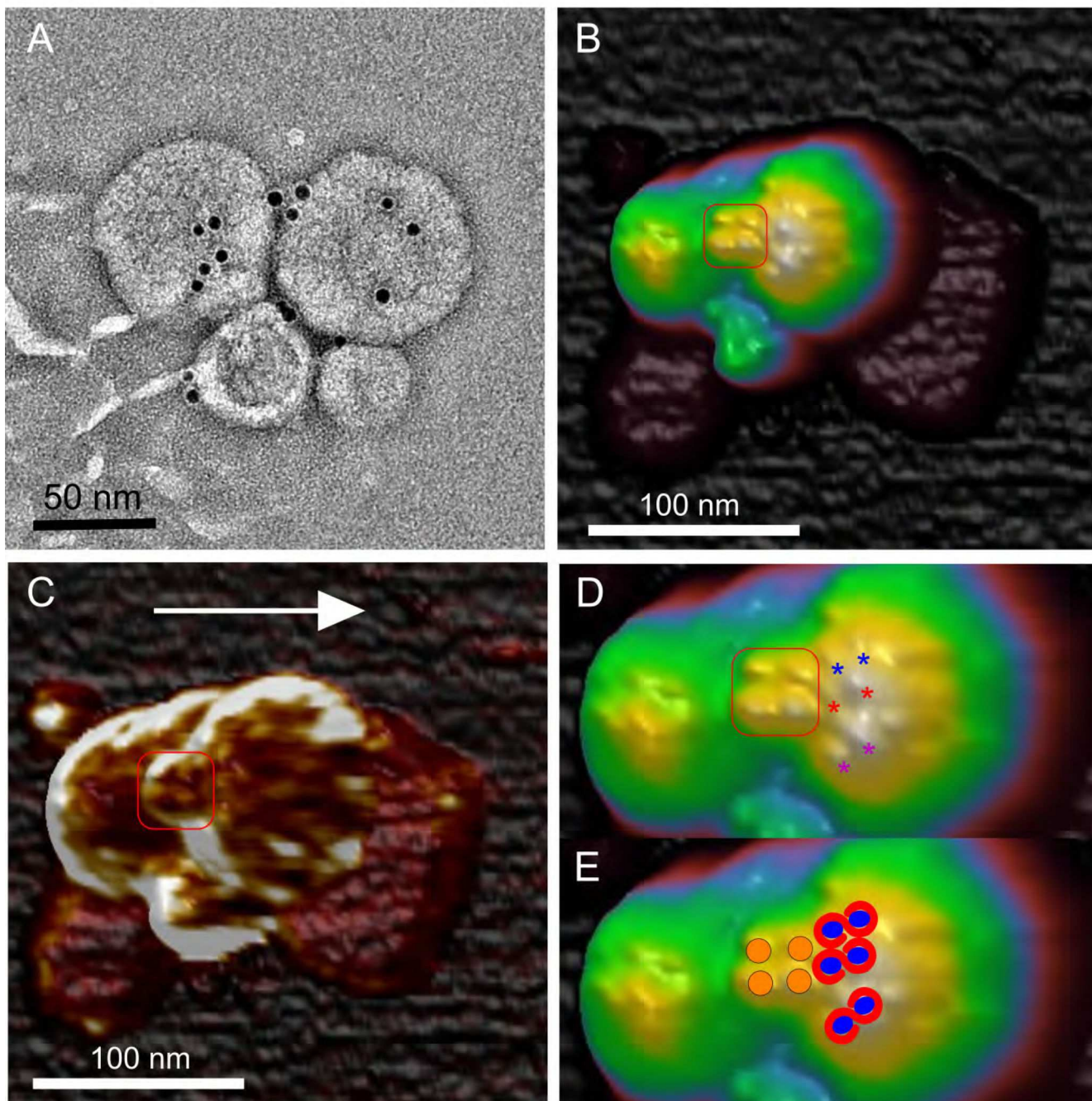


Fig. 3. EM and AFM analysis of intact chromaophores labelled with nanogold

A. Negative stain EM image of a cluster of nanogold labelled chromatophores. B. False colour 3-D representation of AFM data of nanogold labelled chromatophores under liquid, filtered to reduce noise. The red box indicates four putative nanogold beads. The low lying features that extend from the cluster contain lipid without protein. The data were treated with a low pass filter to reduce noise. C. A 3D representation of the deformation channel data overlaid onto the height data in B. The red box denotes four zones of relatively low deformation; the white areas, which correspond to high deformation and are directed along

the sides of the chromatophores in the scan direction (white arrow), show the highly flexible nature of the uncollapsed chromatophore. The data were treated with a low pass filter to reduce noise. D. Close-up of the image in B with pairs of colored asterisks denoting the H-subunits of RC-LH1-PufX core complexes. E. Interpretation of the AFM data; the 9 nm separation of the peaks highlighted by the pairs of blue, red or magenta asterisks is consistent with the peak-to-peak separation of H-subunits in a RC-LH1-PufX dimer complex. The unknown topological features in the red box are indicated with orange circles.

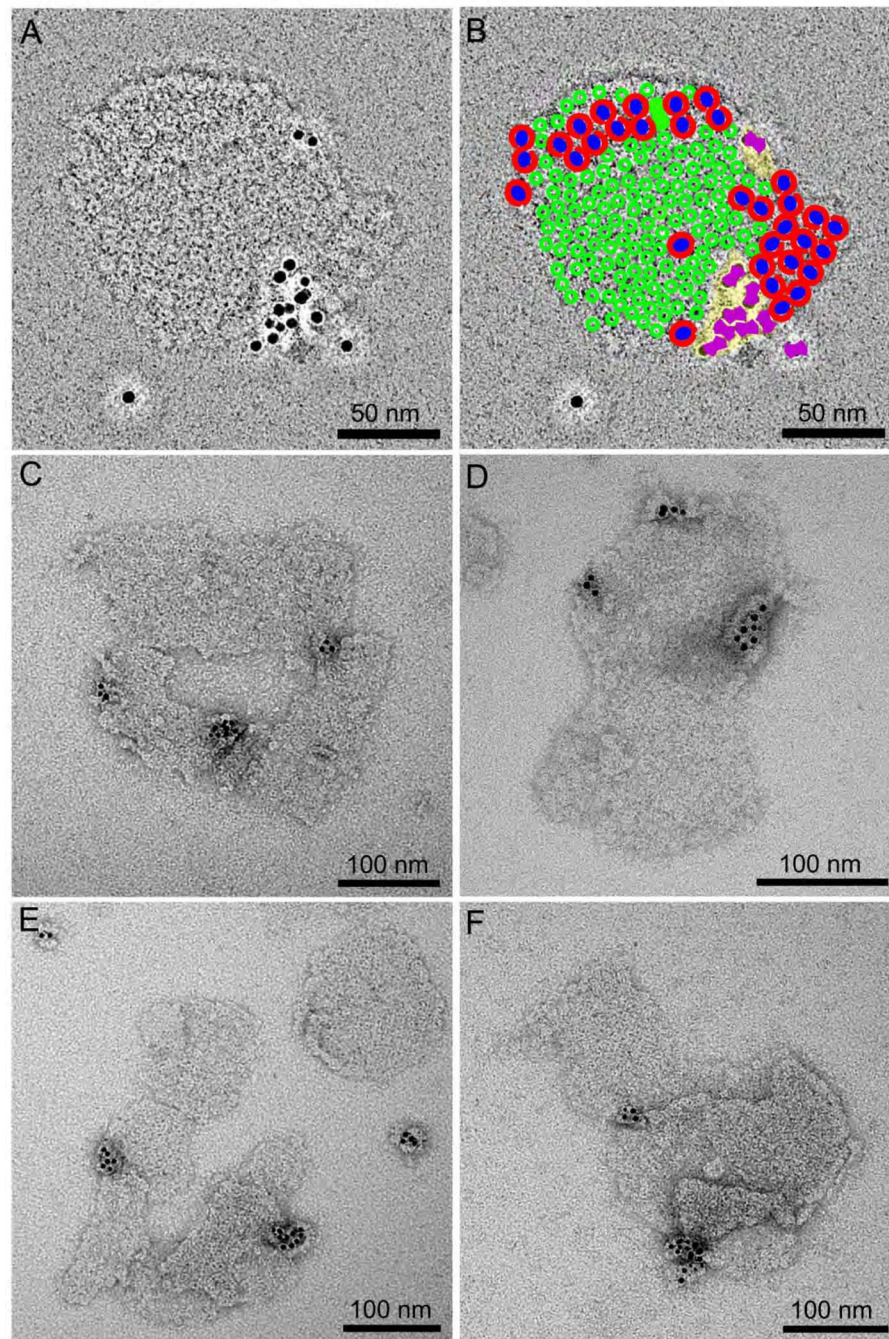


Fig. 4. Negatively stained membrane patches with *cytb*₁ complexes labelled with gold NTA-Nanogold[®]
 A. Patch consisting of one membrane bilayer with gold-labelled *cytb*₁ complexes. B. Assignment of negatively stained features to LH2 complexes (green), RC-LH1-PufX complexes (red/blue) or *cytb*₁ dimers (purple). C–F. A selection of other negative stained gold-labelled membrane patches showing evidence of LH2 and RC-LH1-PufX complexes.

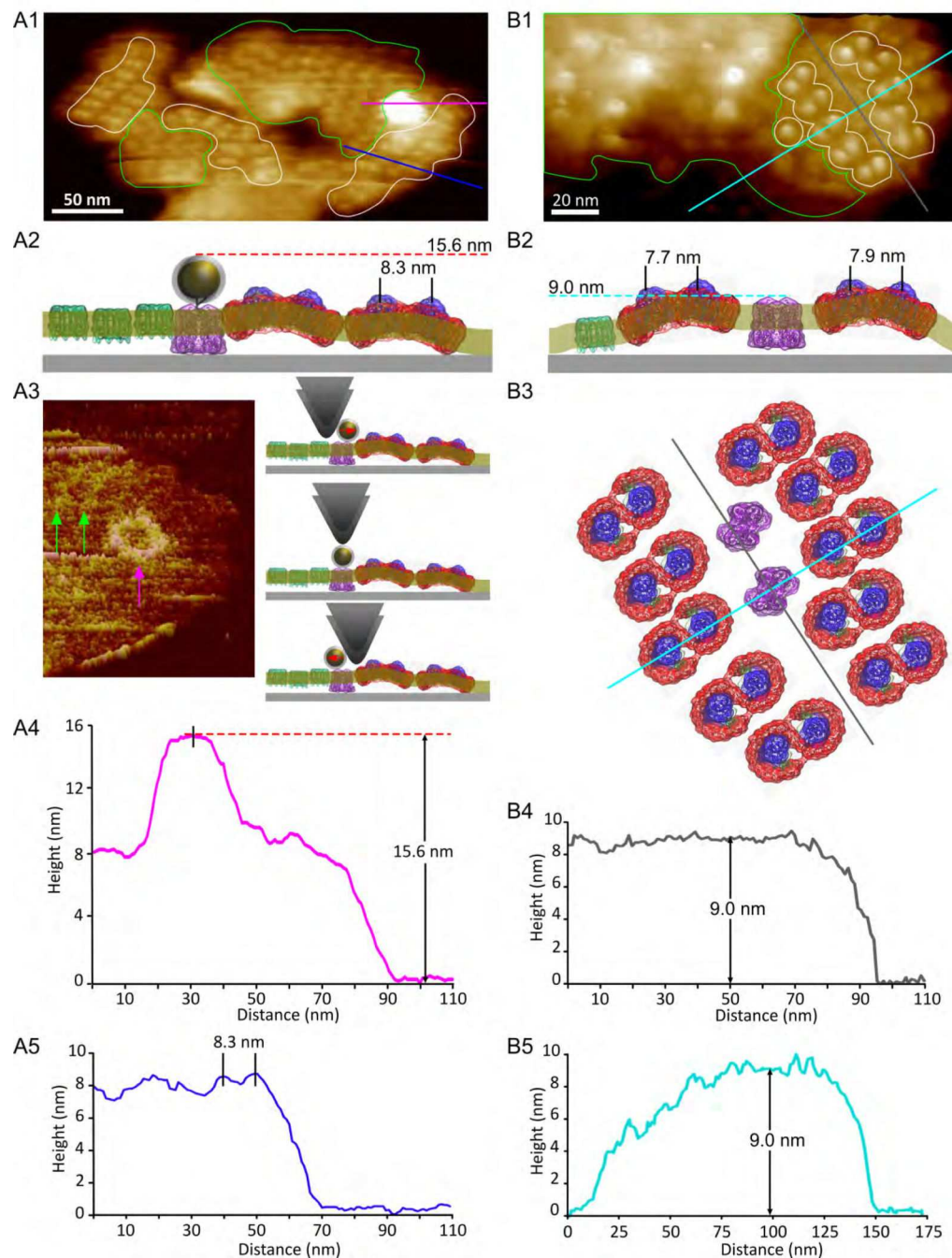


Fig. 5. Comparison of AFM images of a membrane patch containing gold-labelled *cytb*₁ complexes and a non-labeled control patch

A1. 3D view of a gold-labelled patch showing the LH2 regions (green outline) and RC-LH1-PufX dimer regions (white outline). The magenta section across the 15.6 nm-high feature (A4) is compatible with a gold bead atop a *cytb*₁ complex dimer. The blue section shows the 8.3 nm separation (A5) typical of a core dimer. A2. Model of how the complexes reside in the membrane in relation to the mica surface; the large tip convolution prevents direct visualisation of the complexes adjacent to the putative gold label but both zigzags of LH2

and arrays of RC-LH1-PufX dimers can be seen going underneath this feature. A3. Deformation channel data for the image in A1 showing (left) a clear circular feature (magenta arrow) centred on the maximum height of the feature, and (right) a graphic demonstrating how the sides of the AFM tip would initially displace the gold bead laterally, then tap directly down upon it, then push it aside during the scanning process. B1. 3D view of a non-labelled patch with LH2 and RC-LH1-PufX regions denoted by the green and white outlines; no discrete 15.6 nm-high features were observed for any of the unlabelled membrane patches. B2. Graphic demonstrating the co-location of RC-LH1-PufX and *cytbc*₁, showing the curvature of the membrane and the consequent lack of contact of the complexes with the mica substrate. B3. Model of the membrane in B1, showing how *cytbc*₁ can be accommodated between rows of RC-LH1-PufX complexes. B4. Section along the area between rows of cores, putatively containing *cytbc*₁ complexes and corresponding to the gray lines in B1, B3, showing that the cytoplasmic surfaces of the putative proteins are 9 nm above the mica. B5. Section across the area putatively containing *cytbc*₁ complexes and corresponding to the cyan lines in B1, B3, showing that the patch is not flat on the mica but actually curved, probably as a result of the aligned RC-LH1-PufX complexes which are known to curve the membrane.

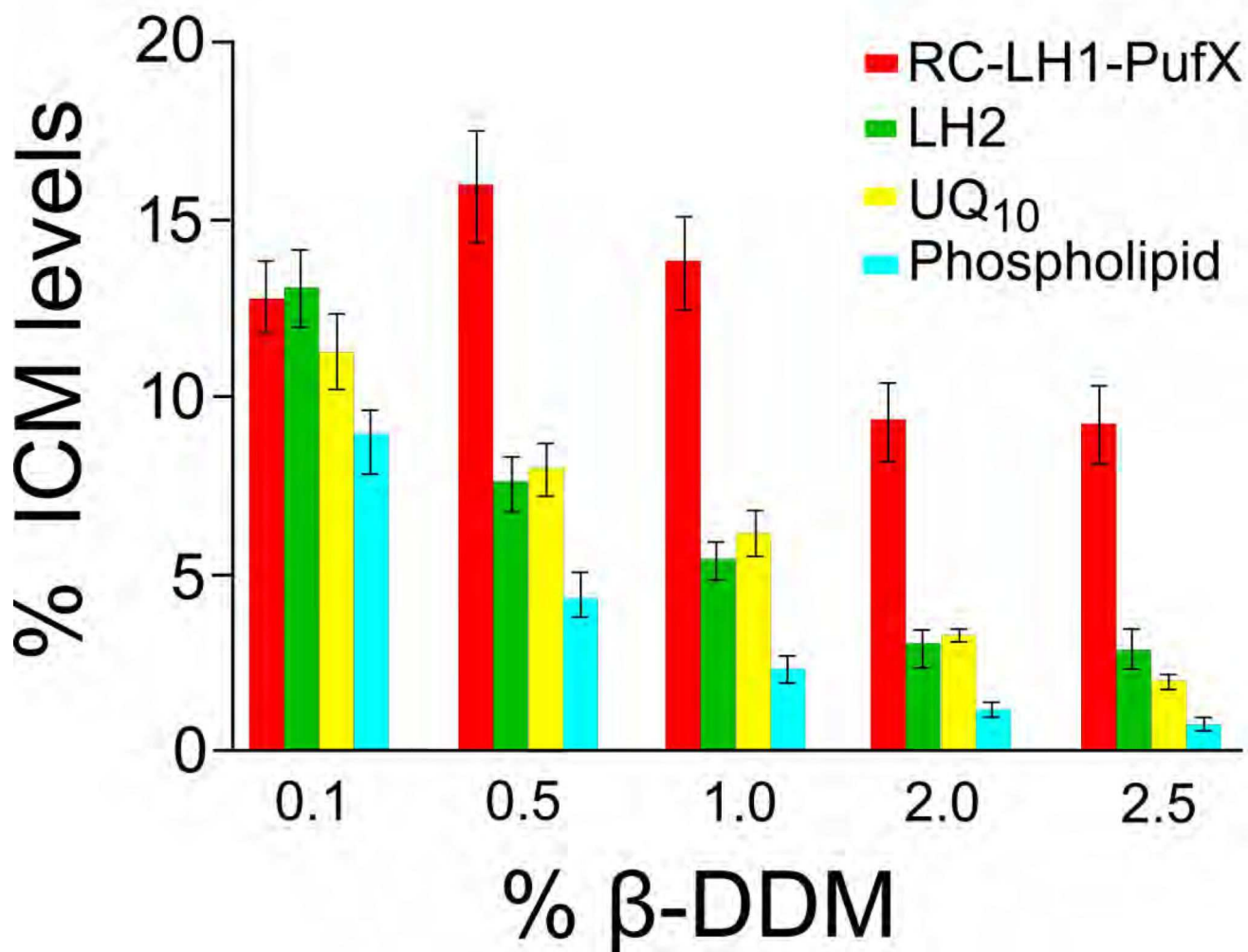


Fig. 6. Selective retention of RC-LH1-PufX complexes following affinity purification of His-tagged *cytb*₁ complexes

All *cytb*₁, LH2, and RC-LH1-PufX levels are expressed as a percentage of the starting molar ratio of each component per *cytb*₁ dimer in the intact membrane (0% β -DDM), as in the first row of Table 2. The error bar is the standard error of the mean. % β -DDM refers to the concentration of detergent used for the initial solubilisation of the membranes (see Methods). All subsequent steps, including washing and elution of the affinity columns, were performed with detergent-free buffer.

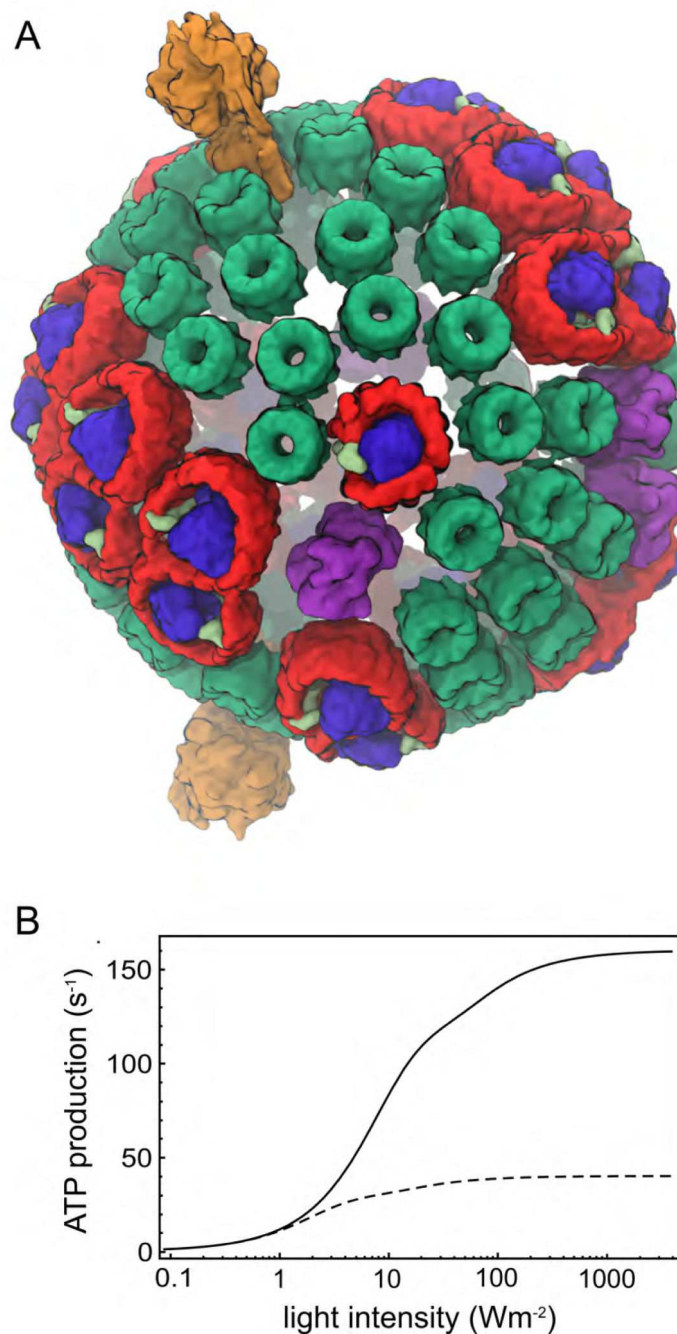


Fig. 7. Atomic structural model of a chromatophore vesicle

A. The vesicle comprises 67 LH2 complexes (green), 11 LH1-RC-PufX dimers & 2 RC-LH1-PufX monomers (blue/red), 4 *cytbc*₁ dimers (magenta), and 2 ATP synthases (orange) (see movie in Supplementary Information). B. ATP production rate for steady state illumination as a function of incident light intensity for the vesicle shown (solid line) and for a reference vesicle containing only one *cytbc*₁ dimer complex but 7 additional LH2 complexes to maintain vesicle surface area (dashed line). At a typical low light intensity of

30 W/m² the vesicle produces 119 ATP/s, the rate increasing slowly to 158 ATP/s at a saturating intensity of 1 kW/m².

Table 1
Quantification of RC, *cytbc*₁, ATP synthase and terminal *cytc* oxidases within chromatophores by mass spectrometry

Chromatophores were co-solubilised with a ¹⁵N-labelled artificial protein standard composed of concatenated sequences of tryptic peptides which are known to represent the target proteins in proteomic analysis. This mixture was subjected to trypsin digestion; each digestion time-point was analysed by nanoLC-MS/MS in duplicate. For each proteotypic peptide, the time-point which gave the highest intensity was used for quantification using the ratio between its (¹⁴N) monoisotopic ion and the ¹⁵N-labelled counterpart at known concentration. Method details are provided in the Methods section and in Supplementary Information. Although some of the peptides had similar quantification results over two or more time-points, only the highest intensity time-point was used in the final dataset. The final numbers for each proteotypic peptide in the Table are the mean of 2 replicates.

Protein	Tryptic peptide	Quantity (nmol/g total protein)	Stoichiometry (ratio per 1 PufM)	Stoichiometry (ratio per 24 PufM)
RC PufM	AEYQNIFSQVQVR	724 ± 1	1.00 ± 0.00	24.0 ± 0.0
RC PufL	ALLSFER	778 ± 112	1.07 ± 0.15	25.8 ± 3.7
<i>Cytbc</i> ₁ FbcC	SLSEPGPELPEDQVR	257 ± 3	0.36 ± 0.00	8.5 ± 0.1
<i>Cytbc</i> ₁ FbcF	SVQLGQLVDTNAR	203 ± 14	0.28 ± 0.02	6.7 ± 0.5
ATP synthase AtpF	LAAAEDQIASAEAGAVR	65 ± 9	0.09 ± 0.01	2.1 ± 0.3
ATP synthase AtpX	SDAAAVDAAVAAR	61 ± 2	0.08 ± 0.00	2.0 ± 0.1
ATP synthase AtpA	GIQAAEISAILK	134 ± 6	0.18 ± 0.01	4.4 ± 0.2
	VVDGLGNPIDGK	143 ± 9	0.20 ± 0.01	4.8 ± 0.2
	TAIALDTILNQK	143 ± 1	0.20 ± 0.00	4.7 ± 0.0
<i>Cytc</i> oxidase CoxII	VVSEEAYAAWLEQAR	0 ± 0	0.00 ± 0.00	0.0 ± 0.0
<i>Cytc</i> oxidase CcoO	AQANPDADTDGLLER	31 ± 0	0.04 ± 0.00	1.0 ± 0.0

Table 2
Quantification of the composition of cytochrome *bc*₁ pulldowns

Rows refer to the molar ratio of a given component per *cytbc*₁ dimer eluted from each affinity column in detergent-free buffer. Membranes were extracted in triplicate with 0.1, 0.5, 1.0, 2.0, or 2.5% β -DDM, then fractionated using a total of 15 affinity columns. Each of the three eluates at a given starting detergent concentration was analysed for complexes or extracted for quinones and lipids in duplicate. The levels of protein complexes in the starting chromatophore vesicles were quantified by mass spectrometry; lipids and quinones were quantified following extraction as detailed in the Methods section. The levels of protein complexes in the affinity column eluates were quantified by absorption spectroscopy, also detailed in the Methods section. The figures in the column are shown with the standard deviation.

Sample	Moles of component per <i>cytbc</i> ₁ dimer			
	RC-LH1-PufX dimer	LH2	Total Lipids	UQ ₁₀
Intact chromatophore	3.4 ± 0.4	21 ± 2.8	4437 ± 677	172 ± 50
0.1% β -DDM	0.43 ± 0.11	2.7 ± 0.7	385 ± 80	19.4 ± 5
0.5% β -DDM	0.54 ± 0.17	1.6 ± 0.5	185 ± 57	13.8 ± 3.8
1.0% β -DDM	0.47 ± 0.15	1.1 ± 0.3	94 ± 32	10.4 ± 3.2
2.0% β -DDM	0.31 ± 0.12	0.60 ± 0.26	46 ± 17	5.5 ± 0.9
2.5% β -DDM	0.31 ± 0.12	0.57 ± 0.37	29 ± 17	3.2 ± 1.1